doi.org/10.26434/chemrxiv.13237373.v1

Computational Modeling Predicts the Stability of Both Pd+ and Pd2+ Ion-Exchanged into H-CHA

Jeroen Van der Mynsbrugge, Martin Head-Gordon, Alexis T. Bell

Submitted date: 14/11/2020 • Posted date: 16/11/2020

Citation information: Van der Mynsbrugge, Jeroen; Head-Gordon, Martin; Bell, Alexis T. (2020): Computational Modeling Predicts the Stability of Both Pd+ and Pd2+ Ion-Exchanged into H-CHA. ChemRxiv. Preprint. https://doi.org/10.26434/chemrxiv.13237373.v1

Passive NO_x adsorbers (PNA) using Pd/zeolites have emerged as a promising solution for the reduction of cold-start emissions from vehicle exhaust. However, the nature of the active sites and the mechanisms underlying NO_x adsorption in Pd/zeolites remain a subject of ongoing investigation. In this study, we employ quantum chemical simulations to investigate the structure of Pd species in cation-exchange sites at isolated Al and Al pairs in the 6-ring and 8-ring of the CHA framework, before the introduction of NO_x. Our calculations show that the speciation of Pd in these exchange sites strongly depends on the precise Al arrangement within the framework, as well as the operating conditions. Ionically dispersed Pd is found to be the most favorable species over a wide range of oxidizing and reducing conditions. Small oligomers of PdO and metallic Pd do not appear to be competitive at either isolated Al or Al pairs. Notably, our calculations show that ion exchange sites other than next-next-nearest neighbor Al pairs in the 6-ring will be preferentially occupied by Pd^{+} instead of Pd^{2+}. The stability of Pd^{+} in the zeolite environment is an interesting contrast with its rareness in molecular Pd compounds. Nonetheless, a detailed analysis of the electronic structure shows that predicted Pd oxidation states are consistent with chemical intuition for all complexes investigated in this study. We also discuss the potential ambiguity in Pd characterization provided by typical experimental techniques such as XANES, EXAFS and UV-VIS, and highlight the need for additional EPR spectroscopy studies to further elucidate the initial Pd speciation in zeolites for PNA applications.

File list (3)

Computational Modeling Predicts the Stability of Both Pd^{+} and Pd^{2+} Ion-Exchanged into H-CHA

Jeroen Van der Mynsbrugge[a], Martin Head-Gordon[b] and Alexis T. Bell[a]*

[a]Department of Chemical and Biomolecular Engineering

University of California, Berkeley, CA 94720, USA

[b]Department of Chemistry

University of California, Berkeley, CA 94720, USA

November 13, 2020

*To whom correspondence should be addressed: alexbell@berkeley.edu

Abstract

Passive NO_x adsorbers (PNA) using Pd/zeolites have emerged as a promising solution for the reduction of cold-start emissions from vehicle exhaust. However, the nature of the active sites and the mechanisms underlying NO_x adsorption in Pd/zeolites remain a subject of ongoing investigation. In this study, we employ quantum chemical simulations to investigate the structure of Pd species in cation-exchange sites at isolated Al and Al pairs in the 6-ring and 8-ring of the CHA framework, before the introduction of NO_x. Our calculations show that the speciation of Pd in these exchange sites strongly depends on the precise Al arrangement within the framework, as well as the operating conditions. Ionically dispersed Pd is found to be the most favorable species over a wide range of oxidizing and reducing conditions. Small oligomers of PdO and metallic Pd do not appear to be competitive at either isolated Al or Al pairs. Notably, our calculations show that ion exchange sites other than next-next-nearest neighbor Al pairs in the 6-ring will be preferentially occupied by Pd^{+} instead of Pd^{2+}. The stability of Pd^{+} in the zeolite environment is an interesting contrast with its rareness in molecular Pd compounds. Nonetheless, a detailed analysis of the electronic structure shows that predicted Pd oxidation states are consistent with chemical intuition for all complexes investigated in this study. We also discuss the potential ambiguity in Pd characterization provided by typical experimental techniques such as XANES, EXAFS and UV-VIS, and highlight the need for additional EPR spectroscopy studies to further elucidate the initial Pd speciation in zeolites for PNA applications.

Keywords

zeolites, passive NO_x adsorbers, emission control, QM/MM, thermodynamics

1 Introduction

In recent years, growing concerns over the detrimental effects of air pollution from the operation of internal combustion engines have led to regulations imposing increasingly stringent limits on the emission of NO_x and hydrocarbons. Further reduction of cold-start NO_x emissions is critical to meeting these new standards. Unfortunately, standard abatement technologies require temperatures above 200°C to function efficiently.[1–3] Passive NO_x adsorbers (PNA) using Pd/zeolites have emerged as a promising solution to the cold-start problem.[4–8] These materials can trap NO at low temperatures, and subsequently release it once the main emission control system has reached its optimal working temperature. The use of Pd-doped MFI, CHA and BEA zeolites as passive NO_x adsorbers was first reported by Johnson Matthey.[4] Pd/zeolites have been found to offer key advantages over related materials such as Pd dispersed on alumina or ceria, including a higher NO trapping efficiency and greater resistance to deactivation by sulfur and hydrocarbon poisoning.[4]

However, the nature of the active sites, and the precise mechanisms underlying NO adsorption in Pd/zeolites and their eventual degradation, remain a subject of ongoing investigation. Such molecular-level insights are key to the selection and design of Pd/zeolites with the required efficiency and durability for implementation in practical PNA applications.

A variety of experimental techniques has been employed in several studies to examine the nature of Pd species exchanged into zeolites either directly by X-ray spectroscopy[9–11] EXAFS[11], or indirectly by H_2 temperature programmed reduction[12–14] and infra-red spectroscopy with CO and NO as probe molecules[11,15–17]. The results of these studies have helped define the species present in Pd/zeolites and their interconversion as a function of temperature and gas composition. When

prepared using typical ion-exchange methods, MFI, CHA and BEA zeolites loaded with ~1 wt% of Pd were found to contain a variety of species, ranging from isolated Pd cations compensating the charges associated with isolated Al atoms (-1) or proximate Al pairs (-2) in the zeolite framework, to differently sized PdO clusters enclosed inside the zeolite pores or deposited on the external surface.[5] More recently, Khivantsev et al. have reported the synthesis of Pd/H-CHA with fully atomic dispersion at Pd loadings of up to 2 wt%.[11] This material was shown to be highly efficient at removing NO_x and CO from a simulated exhaust flow, surpassing the performance and Pd utilization of conventionally prepared Pd/zeolites.[11]

Atomically dispersed Pd species in zeolites are commonly designated as Pd^{2+} cations.[5,11] However, IR spectra of NO adsorbed on Pd/CHA typically show two peaks, around 1848 cm^{-1} and 1808 cm^{-1}, which have been assigned in the literature to "NO on Pd^{2+}" and "NO on Pd^{+}", respectively. The assignment of the higher-wave number band dates back to an early study of Pd/Y zeolites by Che et al., in which a band at 1865 cm^{-1} was assigned to NO on Pd^{2+} species.[15] The assignment of the second band is less definitive, but several studies have reported similar features upon NO adsorption and assigned them to NO adsorption on Pd^{+} and Pd^{2+}.[11,16,17] Khivantsev et al. have also performed DFT calculations to support these peak assignments.[17] These studies suggest that the "NO on Pd+" peak emerges as the oxidation state of some Pd sites changes upon NO adsorption.[5,11,16,17] However, the question remains whether Pd^{+} species might already be present in the as-synthesized Pd/H-CHA. The +2 and +4 oxidation states are most common for Pd compounds,[18] including typical precursors used for the preparation of Pd/zeolites by aqueous ion exchange such as $Pd(NH_3)_4(NO_3)_2$.[12–14] While higher oxidation states (Pd^{6+}) have been reported in organometallic complexes,[19] Pd^{+} and Pd^{3+} compounds are exceedingly rare. Pd^{+} had only been observed in a small number of binuclear Pd complexes,[20] until a family of mononuclear Pd^{+} species

was very recently characterized by Luo et al.[21] In the zeolite literature, Jacquemin et al. have reported the presence of Pd^{+} cations based on observation of EPR signals consistent with the presence of paramagnetic species in their study of the catalytic properties of Pd and Fe-exchanged beta zeolites for toluene oxidation.[22]

In a recent study, Paolucci et al. assessed the speciation of Pd in zeolites under PNA conditions using both experiments and periodic DFT calculations.[23] For Pd/H-CHA, these authors conclude that at typical loadings, Pd will occur as Pd^{2+} at specific proximate Al pairs (next-next-nearest neighbors, separated by two Si atoms) in the 6-ring on the basis of the favorable energetics of Pd^{2+} at this ion-exchange site, combined with a model for the Al distribution in CHA introduced in previous work.[24] It is notable, though, that there is still no general consensus in the literature about the Al distribution in CHA, or the abundance of specific proximate Al pairs, which are determined by the Si/Al ratio and the energetics of the interaction between the framework and the structure-directing agent during the zeolite synthesis process.[25] While Al pairs in the 6-ring are often recognized as the most stable sites for cation exchange in CHA, Al pairs in the 8-ring may also stabilize divalent cations. Göltl et al. have reported that the stability of Cu^{2+} and Co^{2+} at Al pairs in the 6-ring and 8-ring depends on the temperature and the partial pressure of water.[26–29] Mlekodaj et al. have shown that in CHA with a Si/Al ratio of 12, Al pairs in the 8-ring separated by up to three Si atoms can also host Co^{2+} cations, especially when solvated with water molecules.[30]

In this study, we have employed quantum chemical simulations to investigate the structure and relative stability of various previously proposed Pd species in cation-exchange sites in CHA in order to elucidate the nature of the adsorption sites available *before* the introduction of NO or other redox-non-innocent molecules that may be present under PNA conditions. Both univalent and divalent species were considered at isolated Al atoms as well as different proximate Al pairs in the

6-ring and 8-ring of the CHA framework (Table 1). Pd/H-CHA is ideally suited for a fundamental study because all T-atoms in the CHA framework are crystallographically identical,[31] allowing a systematic exploration of all possible configurations for the various sites. We find that the speciation of Pd in ion exchange sites, and especially the relative stability of Pd^{2+} vs. Pd^{+} cations depends strongly on the operating conditions, as well as the specific arrangement of the framework Al atoms. We also consider how NH_3 introduced along with Pd^{2+} by aqueous ion exchange might facilitate the formation of more stable Pd^{+} species at specific ion exchange sites. Finally, we compare our findings with various experimental characterization studies not relying on probe molecules that have been reported in the literature, and discuss how Pd^{+} species occurring *in addition to* Pd^{2+} might be overlooked by XANES, EXAFS and UV-VIS spectroscopy.

Table 1. Possible Pd species (Pd oxidation state = 0, 1, 2) present at cation-exchange sites associated with isolated Al atoms and proximate Al pairs in CHA

Pd ox. state	isolated Al	proximate Al pair
-	HZ	HZ HZ
0	Pd_n^0 HZ ↔ PdH^+ Z^- (n=1-4)	HZ Pd_n^0 HZ (n=1-4)
+1	$Pd^+(H_2O)_n$ Z^- (n=0-2)	HZ $Pd^+(H_2O)_n$ Z^- (n=0-2) Z^-Pd^+ Pd^+Z^-
+2	(PdO) HZ ↔ $PdOH^+$ Z^-	Z^- $Pd^{2+}(H_2O)_n$ Z^- (n=0-4) HZ (PdO) HZ ↔ HZ $(PdOH)^+$ Z^- HZ $(PdO)_2$ HZ ↔ Z^- $(PdOH)_2^{2+}$ Z^- Z^- $(Pd\text{-}O\text{-}Pd)^{2+}$ Z^-

2 Models and Methods

2.1 Zeolite model

A large cluster model containing 696 tetrahedral atoms (T696) is used to represent the zeolite topology. The crystallographic structure of CHA was taken from the database maintained by the International Zeolite Association (IZA).[31] The cluster model was formed by selecting all framework atoms within a 25 Å radius of a central *cha* cage containing the active site, and trimming the edges of the resulting fragment to obtain a cluster terminated by double six-ring units. This large model avoids any boundary effects and prevents the introduction of unintended anisotropy in the description of long-range interactions.[32]

To model univalent species, a single Al atom was placed in the double six-membered ring at the bottom of the central *cha* cage. Divalent cation-exchange species associated with pairs of framework Al atoms were investigated. In the 6-ring, two cases with different Al-Al distances were examined: a next-nearest neighbor (NNN) pair, in which the two framework Al atoms are separated by one framework Si atom and a next-next nearest neighbor (NNNN) pair, in which the two framework Al atoms are separated by two framework Si atoms. To create the pair sites in the 6-ring, an additional Al atom was inserted in the 6-ring in an NNN or NNNN position relative to the first Al. Additionally, three Al pairs in the 8-ring were created by inserting the second Al atom in the adjacent 8-ring, separated from the first by up to three Si atoms (next-next-next-nearest neighbors or NNNNN) The location of the 6-ring and 8-ring in the central *cha* cage is highlighted in Figure 1.

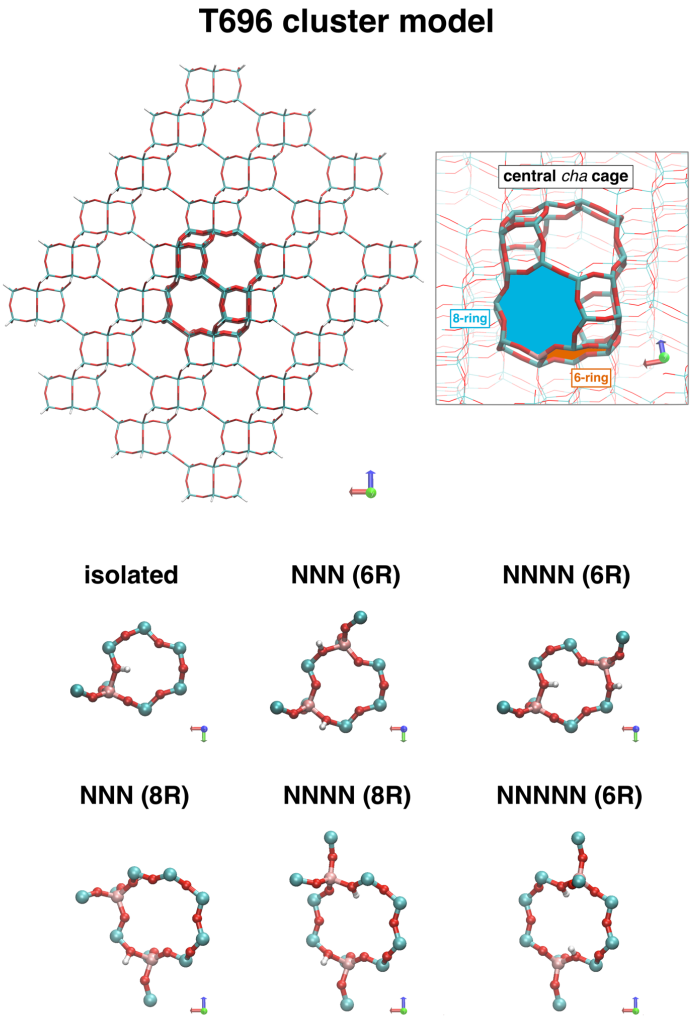

Figure 1. Top left: T696 cluster model for CHA used in QM/MM calculations. Heavier lines highlight the central *cha* cage in which the active sites are placed. Top right: Close up view of the central *cha* cage showing the location of the 6-ring and 8-ring. Bottom: QM regions (8-12 T-atoms) used to model active sites at isolated Al and different proximate Al pairs in the 6-ring (NNN and NNNN) or 8-ring (NNN, NNNN and NNNNN). Si atoms are shown in cyan, Al in pink, O in red, H in white

2.2 QM/MM calculations

A hybrid quantum mechanics/molecular mechanics (QM/MM) approach is applied to limit the computational cost. A smaller cluster containing the active site is treated quantum mechanically (QM), and the remaining framework atoms are treated using molecular mechanics (MM).[33,34] The

Pd species and (where applicable) their hydration shells are always treated at the QM level. For the zeolite support, the complete 6-ring or 8-ring in which the Al atom(s) are located is included, as well as any Si atoms outside the ring that also neighbor an Al atom, are included in the QM region. This leads to QM regions comprising 8 T-atoms for the isolated Al in the 6-ring, 10 T-atoms for Al pairs sharing a 6-ring, and 12 T-atoms for Al pairs sharing an 8-ring. The QM regions used to model the isolated Al and Al pairs are shown using a ball-and-stick representation in Figure 1. The selection of the QM regions used in our study is mainly motivated by the need to describe all specific interactions (other than long-range electrostatics and dispersive interactions) between Pd species, adsorbates and the zeolite at the QM level. In their study of metal dimer sites in Cu-MFI, Arvindsson et al. compared adsorption energies obtained with gas-phase cluster models of increasing size to those calculated with a fully periodic model, and found that a "ring model", which includes the entire 10-ring in which the Al atoms are located, provides a good compromise between accuracy and computational cost.[35] Shor et al. explored the effect of QM region size in a QM/MM model for on the energetics of adsorption complexes of water and Rh_6 in H-FAU.[36] These authors reported that a small QM region consisting of 5 T-atoms was sufficient to capture the structure of Brønsted sites and adsorbed Rh_6 species, while describing the structure and energetics of hydrated complexes required larger QM regions (8 to 14 T-atoms) to account for additional hydrogen bonding interactions with the framework.[36] The QM regions selected in the current study fulfill both of these criteria. As an *a posteriori* validation of the choice of QM region, all optimized geometries were carefully inspected to ensure that all crucial chemical interactions are represented within the QM subsystem. XYZ coordinates of all optimized geometries are included in the ESI. Finally, additional test calculations were performed in which the 6-ring and 8-ring are *both*

included in the QM region to ascertain that our final conclusions are unaffected by our choice of the size of our QM region (see Section S3 in the ESI).

The active sites and adsorbates are described using the ωB97X-D functional[37,38], combined with def2 basis sets[39], which include an effective core potential for Pd. The ωB97X-D functional is a dispersion-corrected, range-separated hybrid functional, which was found to be one of the best performers out of a test set of 53 hybrid GGA functionals in an extensive benchmarking study by Mardirossian and Head-Gordon.[40] Geometry optimizations and frequency calculations are performed at the ωB97X-D/def2-SV(P) level of theory, followed by single-point energy refinements at the ωB97X-D/def2-TZVPD level of theory. Additional test calculations were performed using the range-separated hybrid meta GGA functional ωB97M-V[41], which has emerged as the overall best performer out of the 200 density functionals evaluated by Mardirossian and Head-Gordon[40] to ensure the robustness of our findings with regard to density functional choice. (see Section S4 in the ESI).

The MM region is described with a CHARMM-type force field using the P2 parameters for the zeolite Si and O atoms.[34] The P2 forcefield parameters used to describe the bulk of the zeolite at the MM level were calibrated on the basis of both QM calculations and experimental adsorption data, and have been tested extensively in previous work.[34] The zeolite atoms included in the MM region are fixed at their crystallographic positions, and the cluster is terminated by hydrogen atoms to saturate all dangling bonds.

Initial geometries were constructed with ZEOBUILDER.[42] All QM/MM calculations were performed with a developmental version of Q-Chem.[43] Enthalpy and entropy corrections were derived from a normal mode analysis on the various stationary points obtained from QM/MM to calculate free energy values under operating conditions. The quasi-rigid rotor/harmonic oscillator

approximation (RRHO) was used, which applies an interpolation between a one-dimensional free rotor to capture the thermochemical contributions from the low-frequency modes more accurately.[34,44]

3 Results and Discussion

3.1 Model structures for Pd exchange sites in CHA

For each of the possible site topologies for Pd exchange sites listed in Table 1, several chemically equivalent yet structurally different configurations can occur within the zeolite, which may vary significantly in energy. Therefore, an extensive configurational search (see Section S1 in the ESI) was performed in order to identify the lowest free energy structure for each candidate species at isolated Al and NNN and NNNN proximate Al pairs in the 6-ring. Figures 2 and 3 depict these lowest free energy structures of Pd^0—H^+, Pd^+ and $(PdOH)^+$ at the isolated Al, and Pd^0—H^+/H^+, Pd^+/H^+, Pd^{2+}, $(PdOH)^+/H^+$, $(PdOH)_2{}^{2+}$ and $(Pd\text{-}O\text{-}Pd)^{2+}$ at the NNN and NNNN Al pairs. Relative free energies for alternative structures explored in the configurational search are included in Table S1 of the Supplementary Information, highlighting the significant variations (up to ~50 kJ/mol) in free energy between the most and least stable configurations of the various sites. Khivantsev et al. have reported characteristic Pd-O distances in Pd^{2+}, Pd^+H^+ and $(Pd\text{-}O\text{-}Pd)^{2+}$ structures at the NNNN Al pair in the 6-ring obtained using periodic DFT calculations with the PW91-D2 functional.[17] In their recent study, Paolucci et al. have also reported Pd-O distances in Pd^{2+} and Pd^+ complexes in CHA.[23] Comparing the Pd-O distances in our model structures with those reported by Khivantsev et al.[17] and Paolucci et al.[23] shows excellent agreement despite the use of different computational protocols (see Table S2 in the ESI).

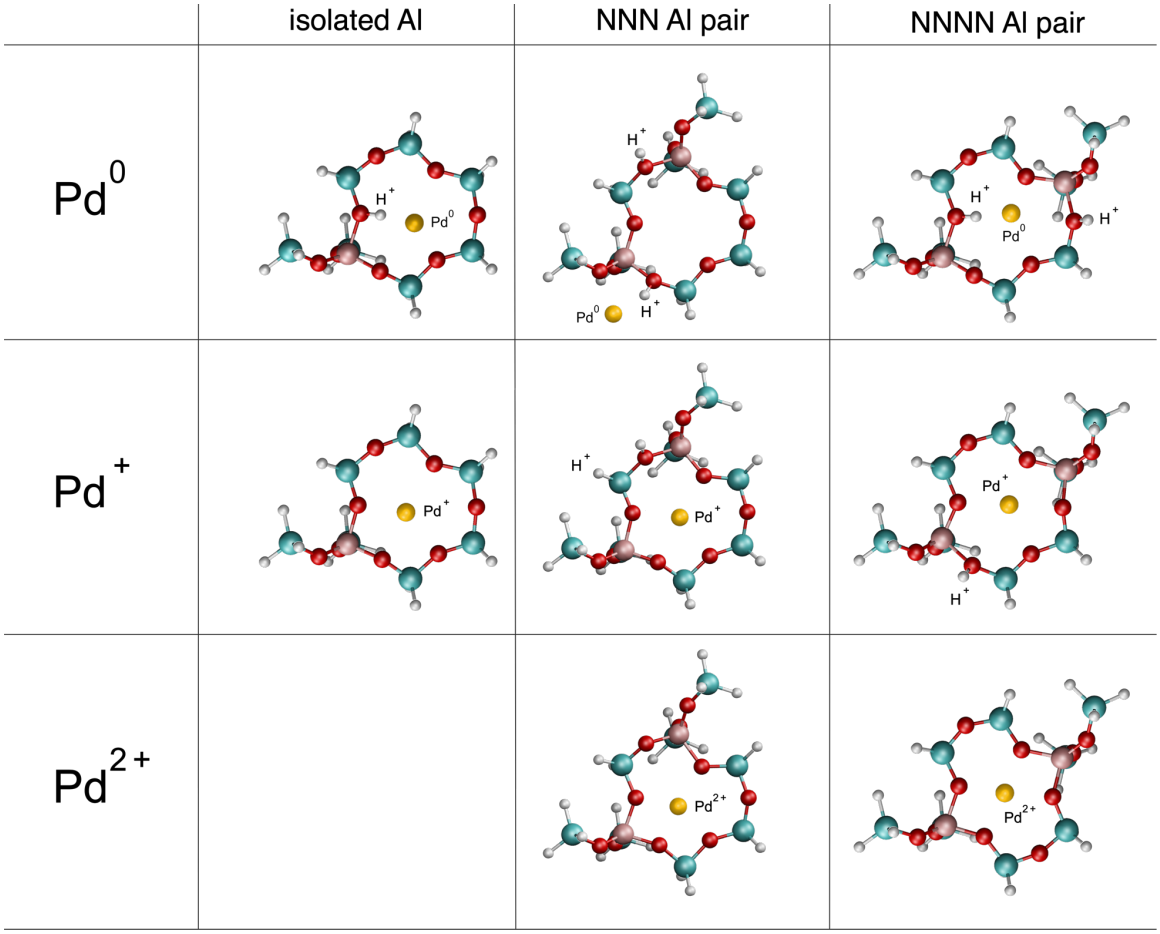

Figure 2. Lowest free energy configurations for Pd^0—H^+ and Pd^+ at the isolated Al, and Pd^0—H^+/H^+, Pd^+/H^+ and Pd^{2+} at the NNN and NNNN Al pairs in the 6-ring in CHA. Si atoms are represented in cyan, Al in pink, O in red, H in white. For clarity, only the small clusters of zeolite atoms included in the QM region are shown.

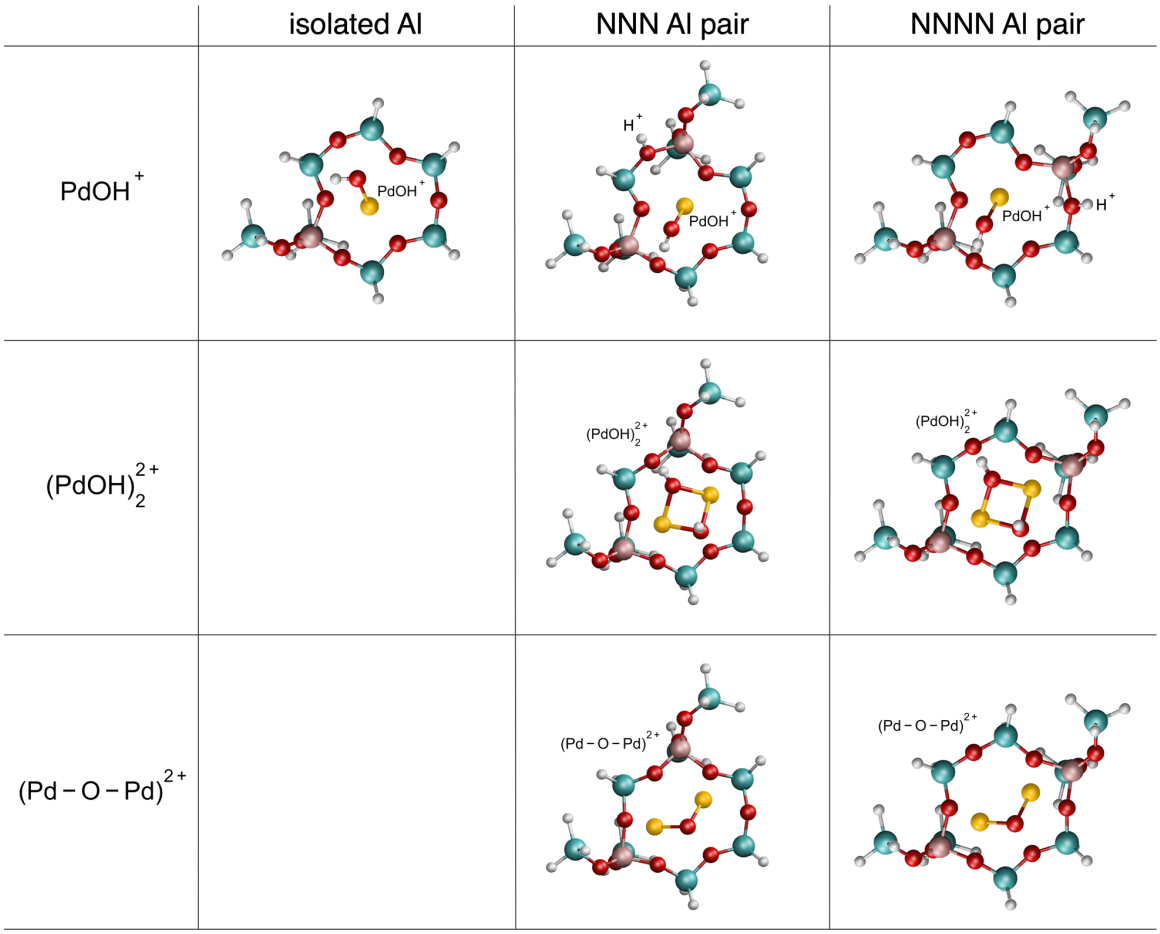

Figure 3. Lowest free energy configurations for $(PdOH)^+$ at the isolated Al, and $(PdOH)^+/H^+$, $(PdOH)_2^{2+}$ and $(Pd\text{-}O\text{-}Pd)^{2+}$ at the NNN and NNNN Al pairs in the 6-ring in CHA. Si atoms are represented in cyan, Al in pink, O in red, H in white. For clarity, only the small clusters of zeolite atoms included in the QM region are shown.

The overall geometric characteristics of the Pd^0, Pd^+ and Pd^{2+} and complexes are relatively independent of their specific environment – isolated Al, NNN or NNNN Al pairs. Pd^{2+} and Pd^+ cations have four framework oxygen atoms in their first coordination shell. The Pd-O distances for Pd^+ are slightly larger (~ 0.2 Å) than for Pd^{2+}. Pd^0 atoms hover above the Brønsted acid protons, and are therefore in less close contact with the framework oxygen atoms. Both PdO monomers (at isolated Al and Al pairs) and dimers (at Al pairs) (n=1,2) undergo protonation upon interaction with the Brønsted acid protons, forming $PdOH^+$ Z^- at isolated Al, and $PdOH^+Z^-$ H^+Z^- or $(PdOH)_2^{2+}Z^-$ Z^- at Al pairs.

3.2 Relative stability under oxidizing conditions

To assess the relative stability of the various Pd species exchanged in CHA, the free energy of formation per Pd atom for each candidate structure was calculated relative to gas phase Pd^0 atoms and a single Brønsted site (at isolated Al) or pair of Brønsted sites (at Al pairs).

Equations 1 and 2 were used to determine the free energy of formation of specific Pd structures under oxidizing conditions:

$$x\,\mathrm{Pd_{(g)}} + \mathrm{HZ} + (0.5\,y - 0.25z + 0.25)\,\mathrm{O_2} + (0.5\mathrm{z} - 0.5)\,\mathrm{H_2O} \rightarrow \left[\mathrm{Pd}_x\mathrm{O}_\mathrm{y}\mathrm{H}_\mathrm{z}\right]^{+}\mathrm{Z}^{-} \quad (1)$$

$$x\,\mathrm{Pd_{(g)}} + \mathrm{HZ\,HZ} + (0.5\,y - 0.25z + 0.5)\,\mathrm{O_2} + (0.5\mathrm{z} - 1)\,\mathrm{H_2O} \rightarrow \left[\mathrm{Pd}_x\mathrm{O}_\mathrm{y}\mathrm{H}_\mathrm{z}\right]^{2+}\mathrm{Z}^{-}\mathrm{Z}^{-} \quad (2)$$

$$\Delta\mathbf{G_{form}}(\boldsymbol{T}, \boldsymbol{P_{O2}}, \boldsymbol{P_{H2O}}) = \frac{\Delta\mathbf{G}_{\boldsymbol{rxn}}(\boldsymbol{T}, \boldsymbol{P_{O2}}, \boldsymbol{P_{H2O}})}{\boldsymbol{x}} \quad [\text{per Pd atom}] \quad (3)$$

While not directly comparable to any experimental observable, these free energies of formation allow a direct comparison of the stability of different Pd species both within the same Al environment, as well as across isolated Al and different Al pairs. By using the originally present Brønsted sites as a baseline, this definition of the free energy of formation explicitly excludes energy differences originating from the positioning of the Al atoms. Because the Al siting itself is determined by the energetics of the interaction between the framework and the structure-directing agent during the zeolite synthesis process,[25] this definition is more suitable for assessing the thermodynamic driving force for the formation of various exchange species.

Figure 4 shows the free energies of formation for all Pd species at isolated Al and proximate Al pairs in the 6-ring at room temperature (300 K, P_{O2} = 20 kPa and P_{H2O} = 5 kPa) and at an elevated temperature corresponding to a typical oxidative pretreatment (1050 K, P_{O2} = 20 kPa and P_{H2O} =

5 kPa), which Ryou et al. have shown to be key to maximize the NO adsorption performance of Pd/H-CHA materials.[6,45]

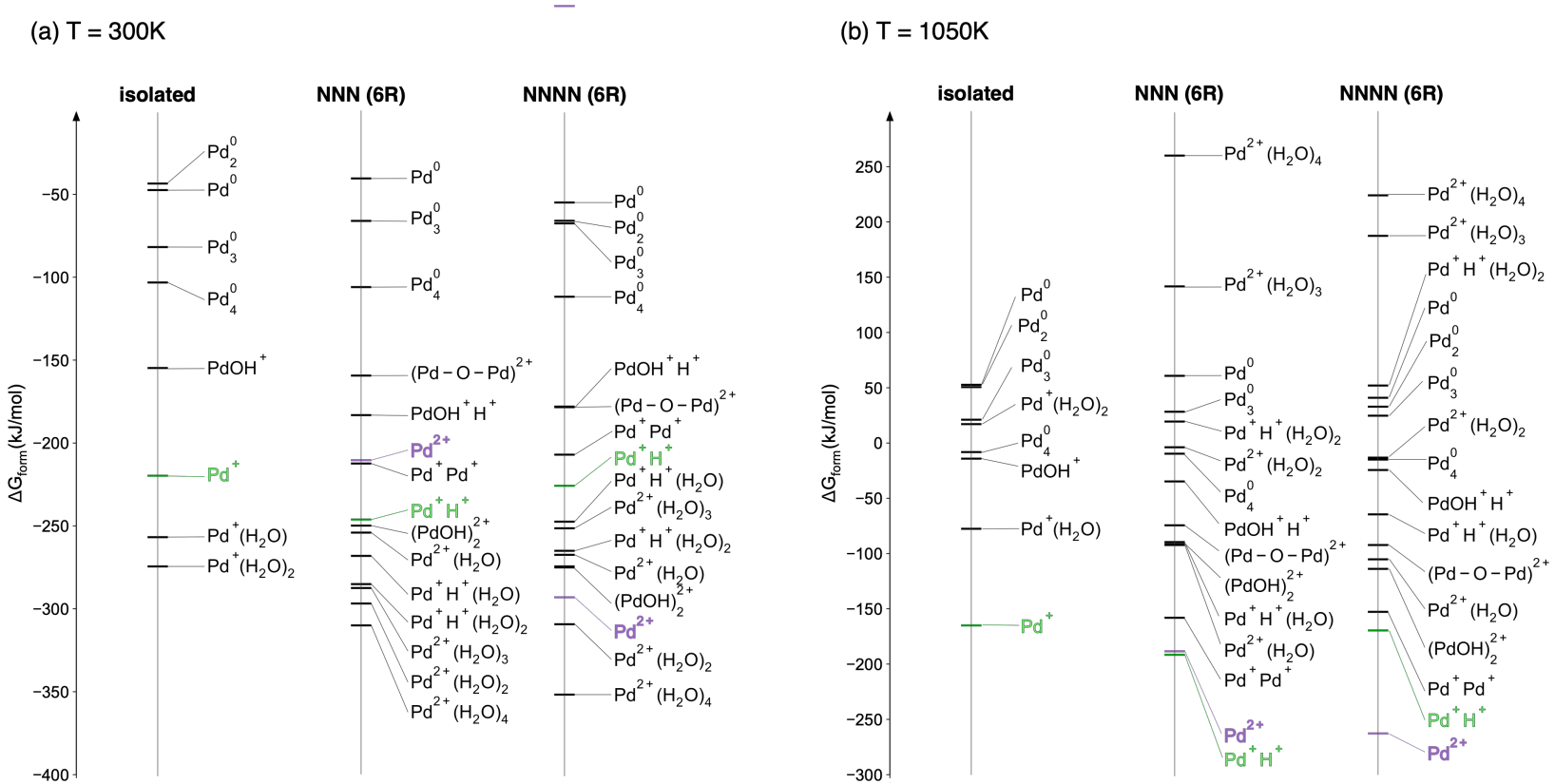

Figure 4: Relative stability of Pd species at isolated Al and proximate Al pairs (NNN and NNNN) in the 6-ring in CHA under oxidizing conditions at 300 K (left) and 1050 K (right). p_{O2} = 20 kPa; p_{H2O} = 5 kPa.

For both sets of conditions, ionically dispersed Pd is more thermodynamically favorable than PdO monomers and dimers at either isolated Al or proximate Al pairs. At room temperature, Pd^{+} and Pd^{2+} are expected to be completely hydrated. Under these conditions, hydrated Pd^{+} or Pd^{2+} species are 60-120 kJ/mol lower in free energy than the most stable PdO monomer or dimer at the same Al configuration. After a high-temperature oxidative treatment, only the bare cations remain, with free energies 100-150 kJ/mol below the most stable PdO species in our dataset. These results are in agreement with XPS measurements on highly-dispersed Pd/H-CHA reported by Khivantsev et al.[17] The side-by-side comparison of the free energies of formation in Figure 4 highlights the exceptional stability of Pd^{2+} at the NNNN Al pair in the 6-ring, which allows for a near-perfect square planar coordination of the Pd^{2+} cation with four framework oxygen atoms (see Figure 2). For the NNN Al pair, the orientation of the zeolite oxygens is less optimal, and Pd^{+} H^{+} emerges as more stable than Pd^{2+}. Paolucci et al. also observed that Pd^{2+} at the NNNN Al pair exhibits a square planar coordination with four Al-connected zeolite oxygens, similar to the common configuration observed in molecular Pd^{2+} complexes, while Pd^{2+} at the NNN Al pair features a less optimal coordination to three Al-connected and one Si-connected oxygens.[23] These authors assessed the preference of Pd^{2+} for different exchange sites by directly comparing the total energies of Pd^{2+} complexes in 25 Al-Al arrangements in CHA, obtained from periodic calculations using the PBE functional.[23] Even though this approach does not exclude energy differences originating from the positioning in the framework of the Al atoms themselves, the authors also found that Pd^{2+} strongly prefers the NNNN Al pair in the 6-ring. This Pd^{2+} complex is 65 kJ/mol lower in energy than next-lowest configuration at the NNN Al pair in the 6-ring.[23] Referring to a previously introduced model of the Al distribution in CHA,[24] Paolucci et al. then argue that CHA materials with typical Si/Al ratios (Si/Al = 5-12) contain sufficient NNNN Al pair sites in the 6-ring to accommodate all Pd

introduced at typical loadings, and therefore other Al pairs need not be considered in CHA. We note, however, there is still no general consensus in the literature about the Al distribution in CHA (and therefore the prevalence of specific Al pairs) and consequently our study examines the relative stability of the candidate species listed in Table 1 at different proximate Al pairs in the 6-rings as well as the 8-rings (see Section 3.4).

To elucidate the relative stability of the various Pd species under a wider range of oxidizing conditions, phase diagrams are constructed by plotting the regions in which specific structures exhibit the lowest free energy of formation as a function of temperature and H_2O partial pressure at a given O_2 partial pressure of 20 kPa, i.e. flowing air (Figure 5).

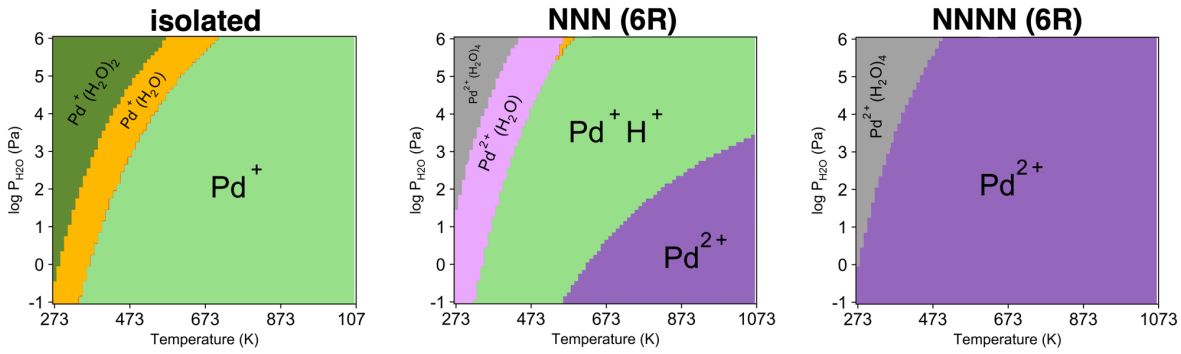

Figure 5. [P_{H2O},T] phase diagrams showing the thermodynamically preferred Pd species at isolated Al and Al pairs – next-nearest neighbors (NNN) and next-next-nearest neighbors (NNNN) – in the 6-ring of H-CHA under flowing air (p_{O2} = 20 kPa).

The phase diagrams shown in Figure 5 reveal that at the NNNN Al pair, Pd^{2+} in its near-perfect square planar coordination with the four Al-connected framework oxygen atoms is more stable than the next most favorable species under most conditions. Figure S6 in the ESI shows the difference in free energy between the most favorable and the next most favorable species, illustrating the uncertainty in the exact delineation between different areas of the phase diagrams. At the NNNN Al pair, Pd^{2+} is more stable than the next most favorable species by >30 kJ/mol over a wide range of conditions, such that it can be considered unchangeable throughout repeated

adsorption-desorption-regeneration cycles on the Pd-CHA samples. On the other hand, at the NNN Al pair, Pd^{2+} or Pd^{+} is preferred depending on the temperature and the partial pressure of water. Since the boundaries between the different areas in the phase diagram are less well-defined, these species may be more easily interconverted (Figure S6).

3.3 Relative stability under reducing conditions

H_2-TPR (temperature-programmed reaction) is frequently employed to characterize the speciation of Pd in zeolites. Homeyer et al. have shown that ionically dispersed Pd in Pd/zeolites can be completely reduced to Pd^0 by exposing the material to H_2 at 250 C.[12–14] To assess the driving force for reduction of Pd^{2+} under these conditions, the free energies of reaction (ΔG_R) for the subsequent reduction steps were calculated at T = 523 K, p_{H2} = 100 kPa and p_{H2O} = 5 kPa:

$Pd^{2+}\ Z^-\ Z^-$ + ½ H_2 → $Pd^{+}Z^-\ H^{+}Z^-$

ΔG_R = -140 kJ/mol (NNN Al pair); -39 kJ/mol (NNNN Al pair)

$Pd^{+}\ Z^-\ H^{+}Z^-$ + ½ H2 → $Pd^0\ H^{+}Z^-\ H^{+}Z^-$

ΔG_R = +68 kJ/mol (NNN Al pair); +105 kJ/mol (NNNN Al pair); + 72 kJ/mol (isolated Al)

These calculations show that while reduction of Pd^{2+} to Pd^{+} appears to be favorable, further reduction of Pd^{+} cations to isolated Pd^0 atoms would not occur. One possible explanation for this discrepancy is that metallic Pd^0 only occurs as small nanoparticles inside the zeolite pores, with the cohesive energy gained in the formation of such nanoparticles tipping the balance of the second reduction reaction in favor of Pd^0. The cohesive energy in bulk Pd amounts to ~31 kJ/mol per Pd-

Pd bond, since each Pd atom has 12 neighbors in the fcc structure.[46] To examine this possibility further, additional structures in which the isolated Pd^0 atom is replaced by small nanoparticles of up to four Pd atoms were included in our study. The structure and relative stability of Pd nanoparticles is a complex problem in its own right, and a comprehensive discussion is beyond the scope of the present study. Several authors have studied the properties of metallic Pd clusters in the gas phase.[47–49] Inside the zeolite framework, the relative stability of these particles was found to be additionally influenced by their specific interactions with the Brønsted sites. Hafner et al. reported that Pd_n (n=1-6) clusters inside mordenite undergo geometric distortions relative to their gas phase structures due both strong interactions with the framework oxygens close to the Al sites and weaker interactions with more distant framework oxygens.[50] In this study, we have limited ourselves to neutral Pd particles of up to four atoms physisorbed at the Brønsted sites in the different Al configurations. The optimized structures for these complexes at the isolated Al are shown in Figure 6.

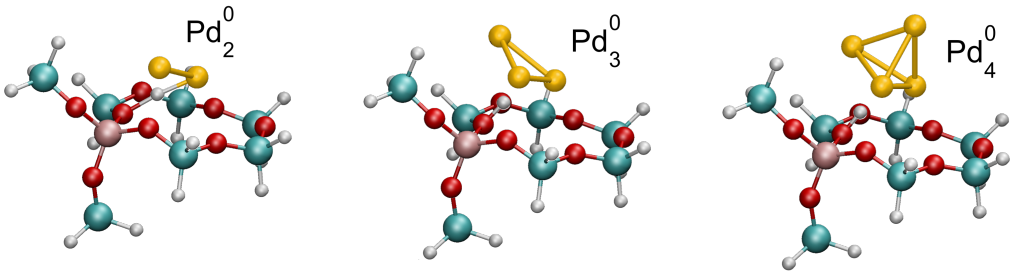

Figure 6. Optimized structures for Pd_n^0 nanoparticles (n = 2-4) interacting with a Brønsted acid proton at an isolated Al in CHA.

Upon interaction with a Brønsted site, Pd particles containing two or more Pd atoms may also protonate to form several variations of $[Pd_nH]^+$ Z^-. In an effort to estimate the additional stabilization that might be gained from protonation, we have evaluated the reaction energy of Pd_n^0

$HZ \leftrightarrow PdH^+ Z^-$ for n=2 and n=4 at the isolated Al. We find that protonation might stabilize Pd_2 by an additional 63 kJ/mol per Pd atom, and Pd_4 by an additional 22 kJ/mol. From Figure 4 it is clear that additional stabilization through protonation by this amount is well short of the relative stability difference between any of the Pd particles and Pd^+/Pd^{2+} cations regardless of the Al arrangement.

Subsequently, phase diagrams under reducing conditions were constructed by plotting the regions in which specific structures exhibit the lowest free energy of formation as a function of temperature, and O_2 or H_2 partial pressure at a given H_2O partial pressure, as defined by Equations 4 and 5:

$$x\,\mathrm{Pd_{(g)}} + \mathrm{HZ} + (0.5\,z - y - 1)\,\mathrm{H_2} + y\,\mathrm{H_2O} \rightarrow \left[\mathrm{Pd}_x\mathrm{O}_y\mathrm{H}_z\right]^+\mathrm{Z}^- \quad (4)$$

$$x\,\mathrm{Pd_{(g)}} + \mathrm{HZ\,HZ} + (0.5\,z - y - 0.5)\,\mathrm{H_2} + y\,\mathrm{H_2O} \rightarrow \left[\mathrm{Pd}_x\mathrm{O}_y\mathrm{H}_z\right]^{2+}\mathrm{Z}^-\mathrm{Z}^- \quad (5)$$

$$\Delta\mathbf{G_{form}}(\boldsymbol{T}, \boldsymbol{P_{H2}}, \boldsymbol{P_{H2O}}) = \frac{\Delta\mathbf{G}_{\boldsymbol{rxn}}(\boldsymbol{T}, \boldsymbol{P_{H2}}, \boldsymbol{P_{H2O}})}{\boldsymbol{x}} \quad [\text{per Pd atom}] \quad (6)$$

The resulting phase diagrams under dry reducing conditions are shown in Figure 7. Heat maps illustrating the uncertainties in the boundary between different areas in the diagrams are shown in Figure S8 in the ESI. The phase diagrams show that $Pd^+ Z^-$ HZ is still the thermodynamically most favorable state under a wide range of conditions. Reduction of Pd^{2+} at the NNNN Al pair is possible, but requires increasing hydrogen partial pressure at above 600 K. While $Pd^0{}_4$ particles are barely competitive at sub-ambient temperatures, and only at very high hydrogen partial pressures. Their appearance in this region of the phase diagram for the NNNN Al pair indicates the existence of a critical size beyond which Pd nanoparticles would resist oxidative redistribution.

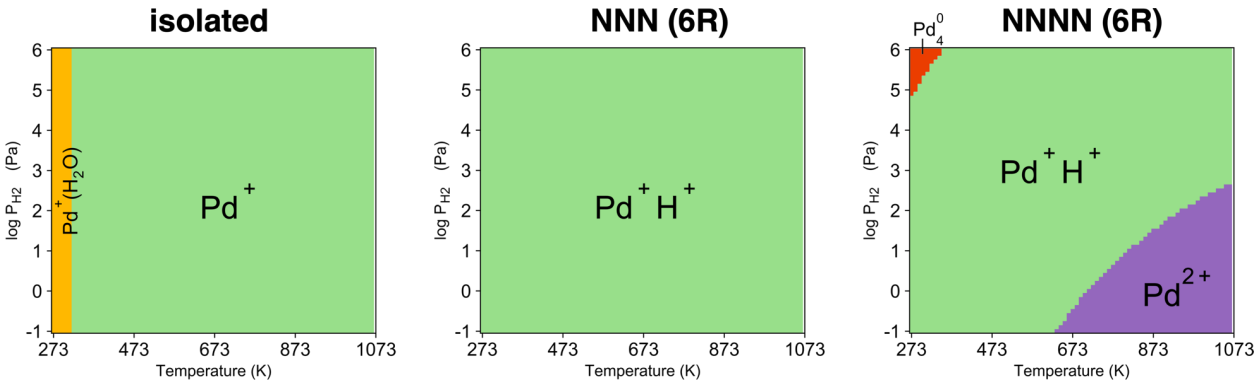

Figure 7. [P_{H2},T] phase diagrams showing the thermodynamically preferred Pd species at isolated Al and Al pairs – next-nearest neighbors (NNN) and next-next-nearest neighbors (NNNN) – in the 6-ring of H-CHA under dry reducing conditions (p_{H2O} = 0.01 Pa).

3.4 Effect of Al-Al distance on stability of Pd species

As mentioned above, while Al pairs in the 6-ring have received the most attention as cation exchange sites in CHA, several authors have shown that Al pairs in the 8-ring could also host divalent cations, depending on the material properties and operating conditions such as temperature and water partial pressure.[26–30] To assess whether such Al pairs may also provide potential NO adsorption sites in Pd/H-CHA, the relative stability of Pd^{+}, Pd^{2+}, and PdO monomers and dimers at three Al pairs in the 8-ring (NNN, NNNN and NNNNN; see Figure 1) was examined, using the same approach as that described in Section 3.2. Figure 8 shows the formation free energies under oxidizing conditions for these species at Al pairs in the 8-ring under ambient conditions (300 K, P_{O2} = 20 kPa and P_{H2O} = 5 kPa) and oxidative pretreatment conditions (1050 K, P_{O2} = 20 kPa and P_{H2O} = 5 kPa). Phase diagrams showing the thermodynamically most stable species as a function of temperature and H_2O partial pressure under flowing air (P_{O2} = 20 kPa) are presented in Figure 9.

Heat maps illustrating the uncertainties in the boundary between different areas are shown in Figure S9 in the ESI. While the stability of Pd^{+} seems to be relatively insensitive to the exact location of the Al or Al pair in either the 6-ring or the 8-ring, the stability of Pd^{2+} in the 8-ring rapidly declines as the distance between the Al atoms increases. Although solvation with water molecules can potentially stabilize the Pd^{2+} at NNNN and NNNNN Al pairs in the 8-ring at 300 K (Figure 8, left), solvation is thermodynamically unfavorable at 1050 K (Figure 8, right), indicating that it is unlikely that (solvated) Pd^{2+} cations remain present in Pd/H-CHA at the end of the high temperature re-oxidation treatment. Both the formation free energies (Figure 8) and the phase diagrams (Figure 9) show that Pd cations are also favored thermodynamically at Al pairs in the 8-ring. At room temperature, Pd^{+} and Pd^{2+} are again expected to be hydrated. Hydrated Pd^{+} and Pd^{2+}exhibit free energies of formation that are up to 120 kJ/mol lower in free energy than the most stable PdO monomer or dimer at the same Al configuration. While fully hydrated Pd^{2+} $(H_2O)_4$ was found to be most favorable at the 6-ring Al pairs under ambient conditions, at the 8-ring Al pairs Pd^{2+} $(H_2O)_3$ is lower in (free) energy. Comparing the minimum energy structures of Pd^{2+} $(H_2O)_3$ and Pd^{2+} $(H_2O)_4$ reveals that the latter complexes are too bulky to fit in the plane of the 8-ring and are therefore unable to maximize hydrogen bonding interactions with the zeolite framework. Comparing the phase diagrams for the 8-ring Al pairs with those for the 6-ring pairs in Figure 5 shows that both Pd^{+} and Pd^{2+} retain at least part of their hydration shell at higher temperatures in the 8-ring compared to the 6-ring, because the larger open space mitigates the entropy losses. Nevertheless, oxidative treatment up to 1050 K will again remove the hydration shells entirely such that only the bare cations remain at the 8-ring Al pairs (Figure 8). As in the 6-ring, Pd^{2+} and Pd^{+} at the NNN Al pair in the 8-ring may be interconverted, depending on the temperature and the water partial pressure. At both the NNNN and NNNN Al pairs in the 8-ring, Pd^{+} H^{+} is preferred

once the hydration shell is driven off. Because of the larger Al-Al distances in the 8-ring (7.20 Å for the NNNN Al pair; 7.84 Å for the NNNNN Al pair) than in the 6-ring (6.20 Å for the NNNN Al pair), the Pd^{2+} cation is unable to efficiently compensate the negative charges associated with both Al atoms at the same time. These findings hint at a critical Al-Al distance (between 6.20 and 7.20 Å) beyond which Al atoms can be expected to behave as isolated for the purposes of stabilizing Pd species.

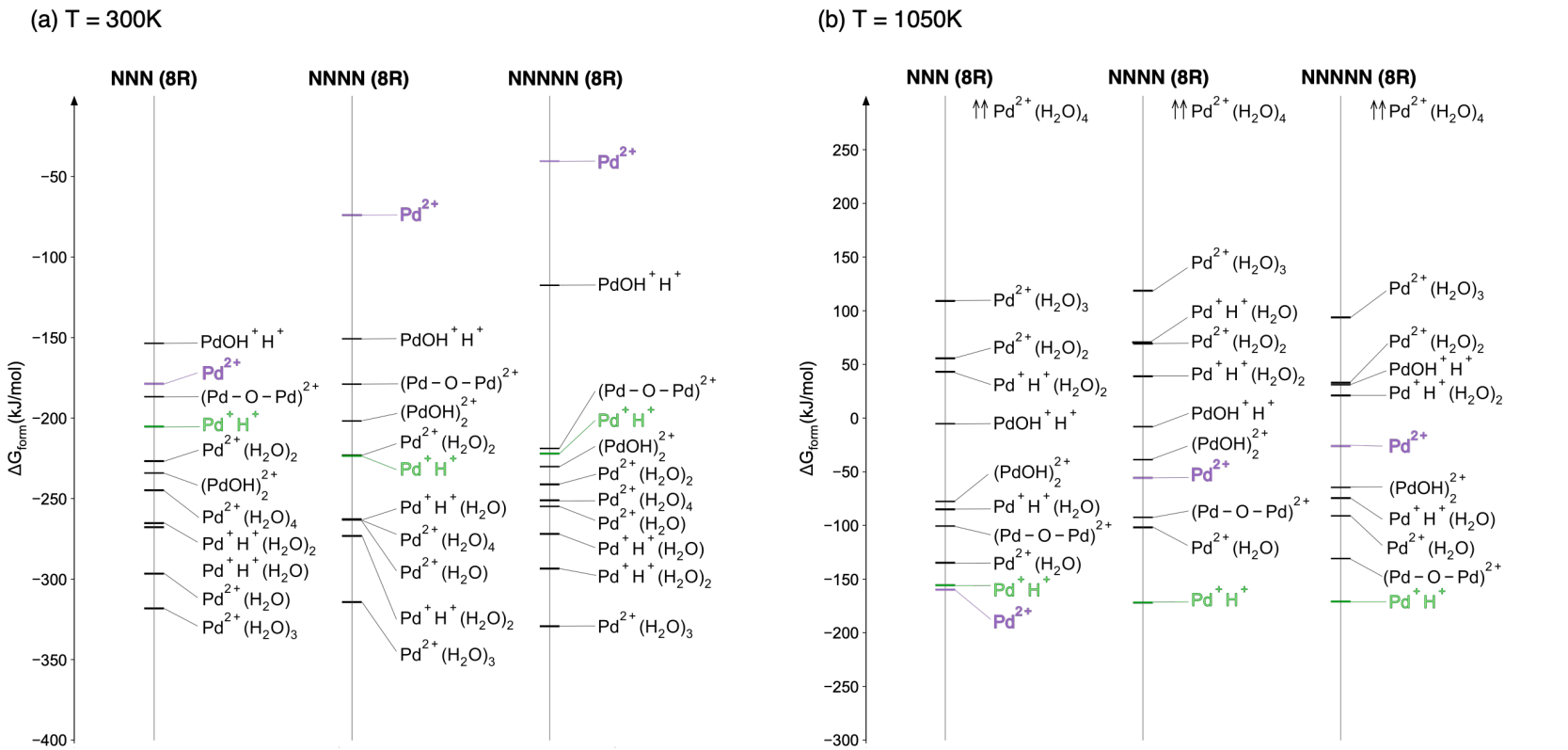

Figure 8: Relative stability of Pd species at proximate Al pairs (NNN, NNNN and NNNNN) in the 8-ring in. CHA under oxidizing conditions at 300 K (left) and 1050 K (right). p_{O2} = 20 kPa; p_{H2O} = 5 kPa.

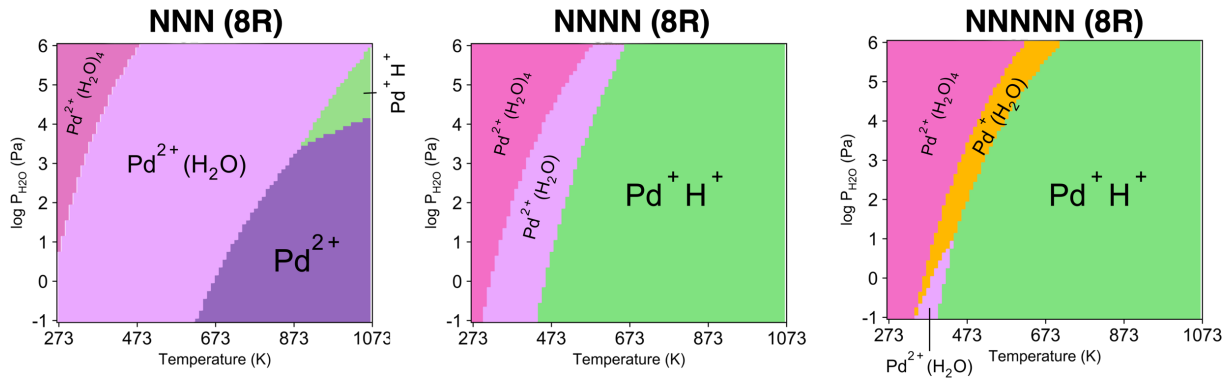

Figure 9. [P_{H2O},T] phase diagrams showing the thermodynamically preferred Pd species at next-nearest neighbor (NNN), next-next-nearest neighbor (NNNN) and next-next-next-nearest neighbor (NNNNN) Al pairs in the 8-ring of H-CHA under flowing air (p_{O2} = 20 kPa).

3.5 Oxidation state of Pd in cation exchange complexes

The oxidation state of the metal center is often used to characterize the catalytic behavior of transition metal complexes. Unlike for simple complexes, the assignment of oxidation state for metal centers in complex environments such as zeolites is not straightforward. Furthermore, from a quantum mechanical perspective, the concept of oxidation states is not well-defined. While atomic charges derived from global population analysis schemes (e.g., Natural Bonding Orbital analysis or NBO[51–53]) can give an indication of the oxidation state of the metal center, these charges are usually lower than the formal oxidation states and can be difficult to interpret. The localized orbital bonding analysis (LOBA) developed by Thom et al.[54] has proven to be a robust and reliable alternative for determining oxidation states consistent with chemical intuition.[54,55]

To verify whether the oxidation state of Pd in the cation exchange complexes identified in this study corresponds to the formal oxidation state expected for these species, we have employed LOBA using Pipek–Mezey (PM) localized orbitals,[56,57] combined with a Löwdin population analysis[58,59] and a localization threshold of 60%. Table 2 shows the natural charges on Pd obtained from NBO alongside the oxidation states obtained using LOBA. The results demonstrate that,

while the natural charges do vary between the different Pd complexes, they are lower than expected and the correlation to the oxidation state of the Pd is not immediately clear. On the other hand, the oxidation states obtained with LOBA are in line with chemical intuition: 0 for $Pd^0H^+H^+$, +1 for Pd^+H^+ and +2 for Pd^{2+}. For $Pd^0H^+H^+$, Pd^+H^+ and Pd^{2+}, all electrons are localized on Pd resulting in d^{10}, d^9 and d^8 electron configurations, respectively. For $PdOH^+$, $(PdOH)_2^{2+}$ and $(Pd\text{-}O\text{-}Pd)^{2+}$, the populations of the bonding orbitals corresponding to the Pd-O bonds show that these bonds are strongly polarized, such that the electrons involved are no longer assigned to Pd, resulting in +2 oxidation state in each of these complexes.

Table 2. Natural charges obtained from NBO analysis and oxidation states determined with LOBA for Pd in various cationic exchange complexes at isolated Al and proximate Al pairs (NNN and NNNN) in the 6-ring in CHA.

	isolated	NNN Al pair	NNNN Al pair	
	Pd natural charge (NBO)	Pd natural charge (NBO)	Pd natural charge (NBO)	Pd oxidation state (LOBA)[a]
Pd^{2+} Z^- Z^-	n/a	1.13251	1.10955	+2
Pd^+ Z^- H^+Z^-	0.82720	0.82084	0.81724	+1
Pd^0 H^+Z^- H^+Z^-	0.18343	0.17001	0.16788	0
$PdOH^+$ Z^-	1.15024	1.12887	1.10567	+2
$(PdOH)_2^{2+}$ Z^- Z^-	n/a	1.03444, 1.04167	1.04556, 1.04547	+2, +2
Pd^+ Z^- Pd^+Z^-	n/a	0.77625, 0.84798	0.86166, 0.80567	+1, +1
$[Pd\text{-}O\text{-}Pd]^{2+}$ Z^- Z^-	n/a	1.05567, 1.09424	1.03178	+2, +2

[a] This oxidation state is attained for each of the applicable environments for which NBO charges are shown.

3.6 Validation of Pd oxidation state

The theoretical prediction that Pd^+ would be thermodynamically preferred at isolated Al and next-nearest neighbor Al pairs over a wide range of oxidizing and reducing conditions may be surprising given the relative scarcity of Pd^+ compounds discussed in Section 1, and the nature of Pd in typical precursors used for aqueous ion exchange, such as $Pd(NH_3)_4(NO_3)_2$.[12–14] Pd introduced by aqueous

ion exchange needs to undergo partial reduction to enable the formation of Pd^{+}. To assess whether the NH_3 that is introduced along with the Pd might drive the reduction of Pd^{2+} to Pd^{+} upon insertion in H-CHA, the free energies of reaction (ΔG_R) for the equilibria were calculated (T = 300 K, p = p_{atm}):

$Pd^{2+}\ Z^{-}\ Z^{-} + NH_3(g) \rightarrow Pd^{+}Z^{-}\ H^{+}Z^{-} + H_2\ (g) + ½\ N_2\ (g)$

ΔG_R = -112 kJ/mol (NNN Al pair); -9 kJ/mol (NNNN Al pair)

$Pd^{+}\ Z^{-}\ H^{+}Z^{-} + NH_3(g) \rightarrow Pd^{0}\ H^{+}Z^{-}\ H^{+}Z^{-} + H_2\ (g) + ½\ N_2\ (g)$

ΔG_R = +130 kJ/mol (NNN Al pair); +94 kJ/mol (NNNN Al pair)

These results indicate that the presence of NH_3 could drive the reduction of Pd^{2+} to the thermodynamically preferred Pd^{+} at isolated Al and NNN Al pairs, even if no additional reducing agents are applied. Note that the complete reduction to atomically dispersed Pd^{0} remains unfavorable and would presumably require the agglomeration of Pd into small particles, as discussed above.

In summary, our calculations strongly indicate that Pd can be present as Pd^{+} in cation exchange sites other than NNNN sites in the 6-ring. In the following sections, we explore how this finding might be corroborated with experimental evidence from various spectroscopic techniques that have been used for the characterization of metal-modified zeolites.

3.6.1 XAS spectroscopy

X-ray absorption spectroscopy has been used to characterize the nature and oxidation state of Pd in Pd catalysts, including Pd/zeolites. Ali et al. collected X-ray absorption spectra of Pd/H-ZSM-5 and Pd/SiO_2 samples before and after complete oxidation (Figure 10, left). While different features emerge in the EXAFS region between the PdO standard and the oxidized Pd/H-ZSM-5 samples, these authors conclude that Pd in H-ZSM-5 is in the metallic state prior to oxidation, and in the Pd(II) state after complete oxidation, on the basis of the apparently very strong agreement between the shape of the XANES edges for the Pd/H-ZSM-5 samples before and after oxidation and those for a Pd foil and for PdO powder, respectively.[9] Okumura et al. performed similar experiments on Pd/H-ZSM-5 before and after interaction with NO (Figure 10, right).[10] The agreement between the XANES edges for Pd/H-ZSM-5 and PdO in their study is less strong, and these authors conclude that Pd in H-ZSM-5 is distinguishable from Pd in PdO. Additionally, there is only a subtle shift in the spectrum for Pd/H-ZSM-5 after NO adsorption, which Okumura et al. characterize as "NO on Pd(I)". These two studies highlight the difficulty in assigning oxidation states to Pd in zeolites on the basis of similarity of the XANES to known standards.

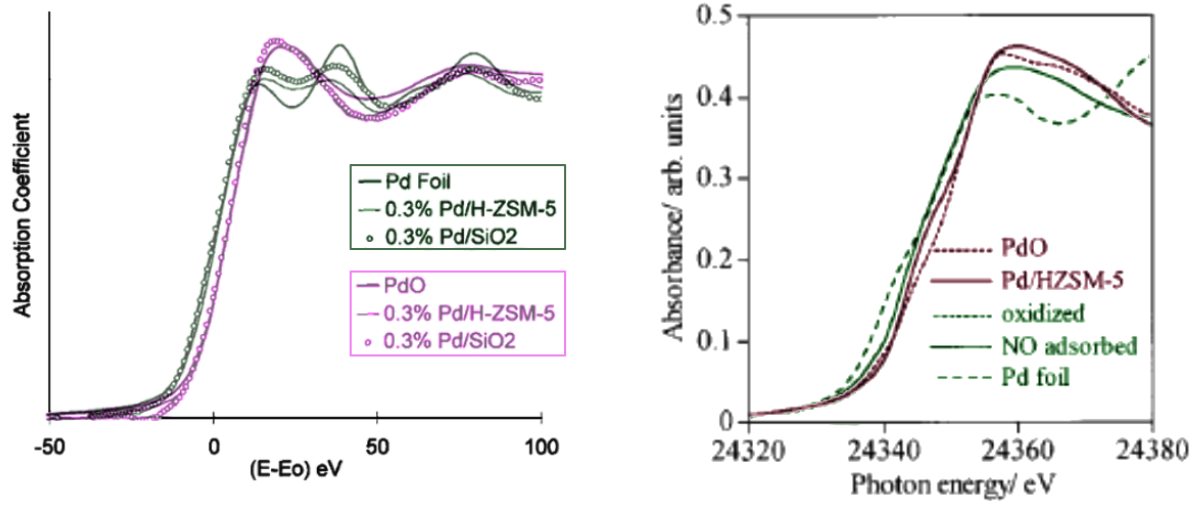

Figure 10: (left) K-edge XANES of Pd/H-ZSM-5 before and after complete oxidation compared to Pd foil as a standard for Pd(0) and PdO as a standard for Pd(II). Adapted from ref. [9] (right) K-edge XANES of Pd/H-ZSM-5 before and after interaction with NO compared to Pd foil as a standard for Pd(0) and PdO as a standard for Pd(II). Adapted from ref. [10]

Figure 11 shows in ascending order, all Pd-O distances in the lowest free energy configurations of Pd^{+} and Pd^{2+} in the 6-ring identified in Section 5.2. This analysis reveals that both Pd^{+} and Pd^{2+} are coordinated to 4 zeolite oxygens in their first coordination shell. The Pd-O distance in this first shell appears to be fairly independent of the exact Al placement, and is found to be slightly longer for Pd^{+} (~2.3Å) than for Pd^{2+} (~2.1Å). However, this difference between Pd^{+} and Pd^{2+} is likely too subtle to resolve in the interpretation of experimental EXAFS signals.

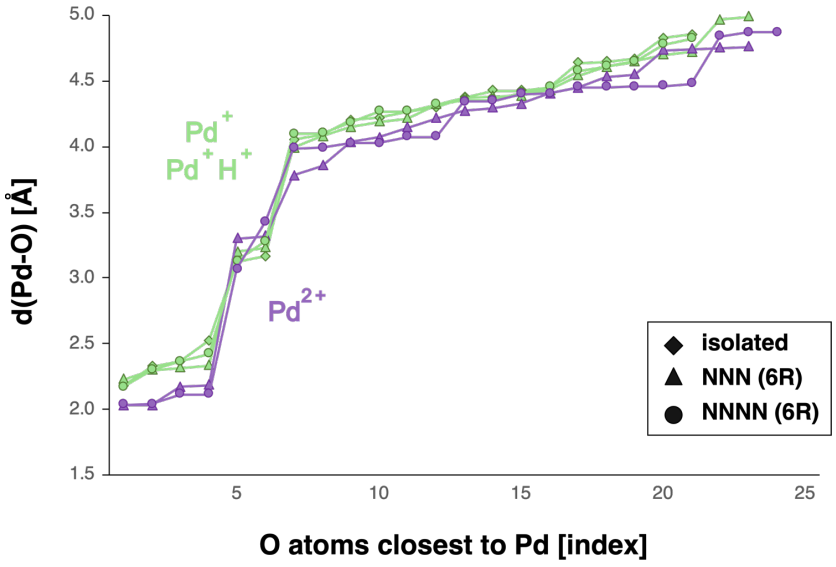

Figure 11. Pd-O interaction distances (in ascending order) in lowest free energy configurations of Pd^{+} sites at isolated Al, and Pd^{+} and Pd^{2+} sites at proximate Al pairs (NNN and NNNN) in the 6-ring in CHA.

3.6.2 UV-VIS spectroscopy

The use of DRUV-VIS spectroscopy to elucidate the nature of the metal species exchanged in zeolites has also been investigated in the literature. While variations in d-d transitions and ligand-to-metal charge transfer among different species can be expected to result in distinct contributions

to measured UV-VIS absorption spectra, an unambiguous identification of these features is not straightforward.[60] Li et al. reported a combined experimental and theoretical UV-VIS study of Cu-SSZ-13.[60] These authors found that even for zeolite samples specifically prepared to favor the presence of certain types of Cu species ($CuOH^+$ or Cu^{2+}), the experimental UV-VIS spectra contain features that are difficult to assign by comparison with calculated spectra, even when thermal dynamics and configurational variations are taken into account.[60] To assess whether UV-VIS measurements could offer corroboration for our prediction based on thermodynamics that Pd^{2+} species are strongly favored only at NNNN Al pairs in the 6-ring, while any other Al arrangement in CHA is likely to favor Pd^+ species, we have calculated UV-VIS spectra for Pd^+ species at isolated Al and NNN and NNNN Al pairs, and Pd^{2+} species at NNN and NNNN Al pairs in the 6-ring using TD-DFT calculations on the respective optimized geometries. The resulting spectra are shown in Figure 12. The calculated UV-VIS spectra for Pd^+ and Pd^{2+} are found to be relatively independent of the precise location of the Al atoms. The spectrum for Pd^+ does not appear to contain any contributions from d-d transitions at wavelengths between 290 and 750 nm. On the other hand, the wavelengths of the characteristic absorption peaks for Pd^+ and Pd^{2+} in the ligand-to-metal charge transfer region are very close. As a result, differentiating between these species on the basis of experimental UV-VIS measurements is likely not possible; the presence of Pd^+ cannot be excluded if a sample also contains Pd^{2+}.

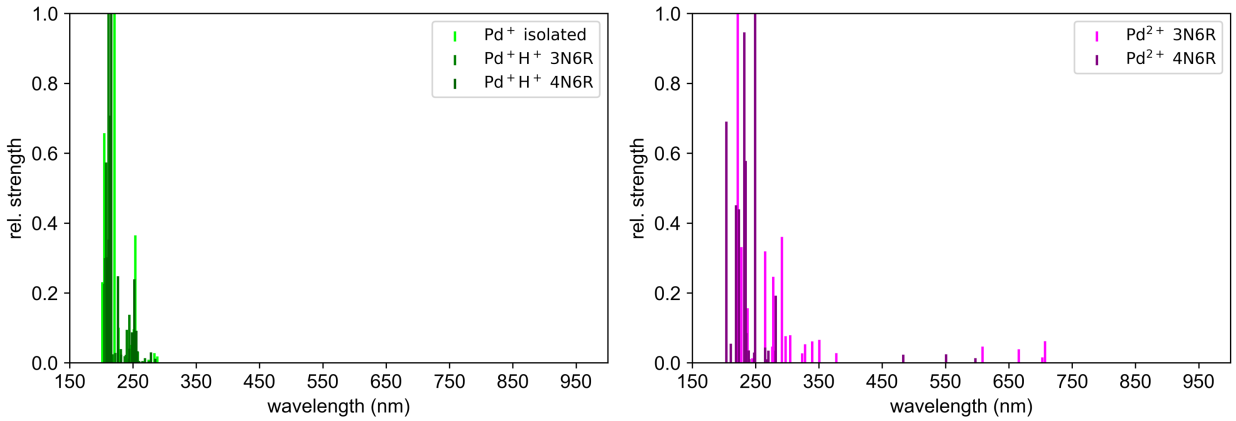

Figure 12. TD-DFT calculated UV-VIS spectra for (left) Pd^{+} at isolated Al and Al pairs (NNN and NNNN) and (right) Pd^{2+} species at Al pairs (NNN and NNNN) in the 6-ring in CHA.

3.6.3 Electron Paramagnetic Resonance spectroscopy

Electron paramagnetic resonance spectroscopy (EPR) has been used to identify and quantify Cu^{+} and Cu^{2+} in Cu/zeolites.[61–63] Diamagnetic Cu^{+} ($3d^{10}$) sites are EPR silent, while paramagnetic Cu^{2+} ($3d^{9}$) sites give rise to characteristic EPR signals, depending on their structural environment (octahedral, square planar, square pyramidal).[61] In Pd/zeolites, Pd^{+} sites ($4d^{9}$) are paramagnetic, and should therefore be observable by EPR spectroscopy. Unfortunately, this technique has not been widely used in studies aiming to characterize Pd/zeolites. A rare exception is found in study of the catalytic properties of Pd and Fe-exchanged beta zeolites for toluene oxidation, in which Jacquemin et al. reported the presence of Pd^{+} species after observing EPR signals consistent with the presence of paramagnetic species.[22] As discussed in the preceding sections, more commonly used characterization methods are likely unable to differentiate conclusively between Pd^{+} and Pd^{2+}. We therefore believe that additional EPR studies of Pd/zeolites are warranted to verify whether at least a fraction of ionically dispersed Pd occurs as Pd^{+}, as predicted by our calculations.

4 Conclusions

We have employed computational methods to examine the relative stability of a variety of monovalent and divalent Pd species at isolated Al and different Al pairs in the 6-ring and 8-ring of the CHA framework. Our calculations show that the speciation of Pd in these exchange sites strongly depends on the precise Al arrangement within the framework, as well as the temperature and gas composition at which Pd/H-CHA is held. Ionically dispersed Pd is found to be most favorable over a wide range of oxidizing and reducing conditions. Pd cations are expected to be fully hydrated under ambient conditions. After treating the material at higher temperatures, the hydration shell is removed resulting in the formation of bare cation sites. Small oligomers of PdO and metallic Pd do not appear to be competitive with Pd cations at either isolated Al or Al pairs.

While NNNN Al pairs in the 6-ring offer exceptional stabilization to Pd^{2+} cations due to a favorable orientation of the surrounding zeolite oxygen atoms, other Al pairs, especially those located in the 8-ring, are unable to provide Pd^{2+} cations with the ideal square planar coordination. Our calculations show that these exchange sites will be preferentially occupied by Pd^{+} and H^{+}. While this finding may be surprising given the relative elusiveness of Pd^{+} in molecular compounds, a detailed analysis of the electronic structure has shown that the oxidation state of Pd in all of the structures investigated in this study is consistent with chemical intuition.

Careful examination of our results in the context of various experimental characterization studies (without probe molecules) reported in the literature shows how Pd^{+} cations occurring in addition to Pd^{2+} cations might be overlooked by XANES, EXAFS and UV-VIS spectroscopy. Assigning oxidation states to Pd in zeolites on the basis of similarity of the XANES to PdO and Pd^{0} standards is not straightforward. While our calculations show that the distance between Pd and the adjacent zeolite oxygens is slightly longer for Pd^{+} than for Pd^{2+}, the difference is likely too

subtle to resolve in EXAFS signals. UV-VIS spectra for Pd^{+} and Pd^{2+} species calculated using TD-DFT were also found to be relatively independent of the precise location of the Al atoms. However, the wavelengths of the characteristic absorption peaks in the ligand to metal charge transfer region for Pd^{+} and Pd^{2+}, respectively, were found to be very close in wavelength, so that unambiguous identification of these species on the basis of experimental UV-VIS measurements is likely not possible. In light of the potential ambiguity in Pd characterization provided by XANES, EXAFS and UV-VIS, EPR spectroscopy may be the only experimental technique to conclusively prove the presence of paramagnetic Pd^{+}, which highlights the need for additional EPR studies of Pd/zeolites to gain detailed insights into the nature of the initially available potential NO adsorption sites.

The predictions from this work showing that Pd^{+} and Pd^{2+} are both present in Pd/H-CHA is interesting and has important implications for understanding the mechanisms underlying NO_x adsorption in Pd/zeolites and the eventual degradation of these materials, which will in turn enable the selection and design of suitable Pd/zeolites for practical PNA applications. Our results set the stage for a careful computational examination of the interaction of NO_x species with the array of Pd^{+} and Pd^{2+} sites that we have predicted to exist in Pd/H-CHA; we hope to report progress on this complex issue in due course.

Conflicts of interest

There are no conflicts to declare.

Acknowledgements

This material is based upon work supported by the U.S. Department of Energy's Office of Energy Efficiency and Renewable Energy (EERE) under the Vehicle Technologies Program Award Number DE - EE0008213. Computational resources were provided by UC Berkeley's Molecular Graphics and Computation Facility (supported by NIH S10OD023532).

Disclaimer

Electronic supplementary information (ESI)

Relative free energies of all structures considered in the configurational search performed to identify the lowest free energy structure for each candidate species at isolated Al and NNN and NNNN proximate Al pairs in the 6-ring; characteristic Pd-O distances for select model structures; validation of the QM region selections used in this work; corresponding electronic energies of formation for the Pd species in the 6-ring and the 8-ring; additional phase diagrams with sensitivity analyses; XYZ coordinates of all stationary points (lowest free energy structures).

5 References

1 P. Forzatti, I. Nova and E.Tronconi, *Ind. Eng. Chem. Res.*, 2010, **49**, 10386–10391.

2 A. M. Beale, F. Gao, I. Lezcano-Gonzalez, C. H. F. Peden and J. Szanyi, *Chem. Soc. Rev.*, 2015, **44**, 7371–7405.

3 C. Lambert and G. Cavataio, Development of the 2010 Ford Diesel Truck Catalyst System BT - Urea-SCR Technology for DeNOx After Treatment of Diesel Exhausts; I. Nova and E. Tronconi, Eds.; Springer New York: New York, NY, 2014; pp 659–689.

4 H.-Y. Chen, J. E. Collier, D. Liu, L. Mantarosie, D. Durán-Martín, V. Novák, R. R. Rajaram and D. Thompsett, *Catal. Letters*, 2016, **146**, 1706–1711.

5 Y. Zheng, L. Kovarik, M. H. Engelhard, Y. Y. Wang, Y. Y. Wang, F. Gao and J. Szanyi, *J. Phys. Chem. C*, 2017, **121**, 15793–15803.

6 Y. Ryou, J. Lee, S. J. Cho, H. Lee, C. H. Kim and D. H. Kim, *Appl. Catal. B Environ.*, 2017, **212**, 140–149.

7 K. Khivantsev, F. Gao, L. Kovarik, Y. Wang and J. Szanyi, *J. Phys. Chem. C*, 2018, **122**, 10820–10827.

8 O. Mihai, L. Trandafilović, T. Wentworth, F. F. Torres and L. Olsson, *Top. Catal.*, 2018, **61**, 2007–2020.

9 A. Ali, W. Alvarez, C. J. Loughran and D. E. Resasco, *Appl. Catal. B Environ.*, 1997, **14**, 13–22.

10 K. Okumura, J. Amano, N. Yasunobu and M. Niwa, *J. Phys. Chem. B*, 2000, **104**, 1050–1057.

11 K. Khivantsev, N. R. Jaegers, L. Kovarik, J. C. Hanson, F. (Feng) Tao, Y. Tang, X. Zhang, I. Z. Koleva, H. A. Aleksandrov, G. N. Vayssilov, Y. Wang, F. Gao and J. Szanyi, *Angew. Chemie Int. Ed.*, **57**, 16672–16677.

12 S.T. Homeyer, *J. Catal.*, 1989, **118**, 266–274.

13 S.T. Homeyer, *J. Catal.*,1989, **117**, 91–101.

14 S. T. Homeyer and W. M. H. Sachtler, *Appl. Catal.*, 1989, **54**, 189–202.

15 M. Che, J. F. Dutel, P. Gallezot and M. Primet, *J. Phys. Chem.*, 1976, **80**, 2371–2381.

16 C. Descorme, P. Gelin, M. Primet, C. Lecuyer, *Catal. Letters*, 1996, **41**, 133–138.

17 K. Khivantsev, N. R. Jaegers, I. Z. Koleva, H. A. Aleksandrov, L. Kovarik, M. Engelhard, F. Gao, Y. Wang, G. N. Vayssilov and J. Szanyi, *J. Phys. Chem. C*, 2020, **124**, 309–321.

18 The Elements Handbook at KnowledgeDoor, http://www.knowledgedoor.com/2/elements_handbook/cohesive_energy.html.

19 R. H. Crabtree, *Science*, 2002, **295**, 288–289.

20 P. L. Goggin and J. Mink, *J. Chem. Soc. Dalt. Trans.*, 1974, **0**, 534–540.

21 J. Luo, G. N. Tran, N. P. Rath and L. M. Mirica, *Inorg. Chem.*, DOI:10.1021/acs.inorgchem.0c01938

22 J. Jacquemin, S. Siffert, J.-F. Lamonier, E. Zhilinskaya and A. Aboukaïs, *Stud. Surf. Sci.*

Catal., 2002, **142**, 699–706.

23 K. Mandal, Y. Gu, K. S. Westendorff, S. Li, J. A. Pihl, L. C. Grabow, W. S. Epling and C. Paolucci, *ACS Catal.*, 2020, **10**, 12801–12818.

24 C. Paolucci, A. A. Parekh, I. Khurana, J. R. Di Iorio, H. Li, J. D. Albarracin Caballero, A. J. Shih, T. Anggara, W. N. Delgass, J. T. Miller, F. H. Ribeiro, R. Gounder and W. F. Schneider, *J. Am. Chem. Soc.*, 2016, **138**, 6028–6048.

25 G. Sastre, V. Fornes and A. Corma, *J. Phys. Chem. B*, 2002, **106**, 701–708.

26 F. Göltl and J. Hafner, *J. Chem. Phys.*, 2012, **136**, 064501.

27 F. Göltl, R. E. Bulo, J. Hafner and P. Sautet, *J. Phys. Chem. Lett.*, 2013, **4**, 2244–2249.

28 F. Göltl, A. M. Love and I. Hermans, *J. Phys. Chem. C*, 2017, **121**, 6160–6169.

29 F. Göltl, P. Müller, P. Uchupalanun, P. Sautet and I. Hermans, *Chem. Mater.*, 2017, **29**, 6434–6444.

30 K. Mlekodaj, J. Dedecek, V. Pashkova, E. Tabor, P. Klein, M. Urbanova, R. Karcz, P. Sazama, S. R. Whittleton, H. M. Thomas, A. V. Fishchuk and S. Sklenak, *J. Phys. Chem. C*, 2019, **123**, 7968–7987.

31 Structure Commission of the International Zeolite Association, Database of Zeolite Structures. http://www.iza-structure.org/databases/

32 E. Mansoor, J. Van der Mynsbrugge, M. Head-Gordon and A. T. Bell, *Catal. Today*, 2018, **312**, 51–65.

33 P. M. Zimmerman, M. Head-Gordon and A. T. Bell, *J. Chem. Theory Comput.*, 2011, **7**, 1695–1703.

34 Y.-P. Li, J. Gomes, S. Mallikarjun Sharada, A. T. Bell and M. Head-Gordon, *J. Phys. Chem. C*, 2015, **119**, 1840–1850.

35 A. A. Arvidsson, V. P. Zhdanov, P.-A. Carlsson, H. Grönbeck and A. Hellman, *Catal. Sci. Technol.*, 2017, **7**, 1470–1477.

36 A. M. Shor, E. A. I. Shor, S. Laletina, V. A. Nasluzov, G. N. Vayssilov and N. Rösch, *Chem. Phys.*, 2009, **363**, 33–41.

37 J. Da Chai and M. Head-Gordon, *J. Chem. Phys.*, 2009, **131**, 174105.

38 J.-D. Chai and M. Head-Gordon, *Phys. Chem. Chem. Phys.*, 2008, **10**, 6615.

39 F. Weigend and R. Ahlrichs, *Phys. Chem. Chem. Phys.*, 2005, **7**, 3297.

40 N. Mardirossian and M. Head-Gordon, *Mol. Phys.*, 2017, 115, 2315–2372.

41 N. Mardirossian and M. Head-Gordon, *J. Chem. Phys.*, 2016, **144**, 0–23.

42 T. Verstraelen, V. Van Speybroeck and M. Waroquier, *J. Chem. Inf. Model.*, 2008, **48**, 1530–1541.

43 Y. Shao, Z. Gan, E. Epifanovsky, A. T. B. Gilbert, M. Wormit, J. Kussmann, A. W. Lange, A. Behn, J. Deng, X. Feng, D. Ghosh, M. Goldey, P. R. Horn, L. D. Jacobson, I. Kaliman, R. Z. Khaliullin, T. Kuś, A. Landau, J. Liu, E. I. Proynov, Y. M. Rhee, R. M. Richard, M. A. Rohrdanz, R. P. Steele, E. J. Sundstrom, H. L. Woodcock, P. M. Zimmerman, D. Zuev, B. Albrecht, E. Alguire, B. Austin, G. J. O. Beran, Y. A. Bernard, E. Berquist, K. Brandhorst, K. B. Bravaya, S. T. Brown, D. Casanova, C.-M. Chang, Y. Chen, S. H. Chien, K. D. Closser, D. L. Crittenden, M. Diedenhofen, R. A. DiStasio, H. Do, A. D. Dutoi, R. G. Edgar, S. Fatehi, L. Fusti-Molnar, A. Ghysels, A. Golubeva-Zadorozhnaya, J. Gomes, M. W. D. Hanson-Heine, P. H. P. Harbach, A. W. Hauser, E. G. Hohenstein, Z. C. Holden, T.-C. Jagau, H. Ji, B. Kaduk, K. Khistyaev, J. Kim, J. Kim, R. A. King, P. Klunzinger, D. Kosenkov, T. Kowalczyk, C. M. Krauter, K. U. Lao, A. D. Laurent, K. V Lawler, S. V Levchenko, C. Y. Lin, F. Liu, E. Livshits, R. C. Lochan, A. Luenser, P. Manohar, S. F.

Manzer, S.-P. Mao, N. Mardirossian, A. V Marenich, S. A. Maurer, N. J. Mayhall, E. Neuscamman, C. M. Oana, R. Olivares-Amaya, D. P. O'Neill, J. A. Parkhill, T. M. Perrine, R. Peverati, A. Prociuk, D. R. Rehn, E. Rosta, N. J. Russ, S. M. Sharada, S. Sharma, D. W. Small, A. Sodt, T. Stein, D. Stück, Y.-C. Su, A. J. W. Thom, T. Tsuchimochi, V. Vanovschi, L. Vogt, O. Vydrov, T. Wang, M. A. Watson, J. Wenzel, A. White, C. F. Williams, J. Yang, S. Yeganeh, S. R. Yost, Z.-Q. You, I. Y. Zhang, X. Zhang, Y. Zhao, B. R. Brooks, G. K. L. Chan, D. M. Chipman, C. J. Cramer, W. A. Goddard, M. S. Gordon, W. J. Hehre, A. Klamt, H. F. Schaefer, M. W. Schmidt, C. D. Sherrill, D. G. Truhlar, A. Warshel, X. Xu, A. Aspuru-Guzik, R. Baer, A. T. Bell, N. A. Besley, J.-D. Chai, A. Dreuw, B. D. Dunietz, T. R. Furlani, S. R. Gwaltney, C.-P. Hsu, Y. Jung, J. Kong, D. S. Lambrecht, W. Liang, C. Ochsenfeld, V. A. Rassolov, L. V Slipchenko, J. E. Subotnik, T. Van Voorhis, J. M. Herbert, A. I. Krylov, P. M. W. Gill and M. Head-Gordon, *Mol. Phys.*, 2015, **113**, 184–215.

44 S. Grimme, *Chemistry*, 2012, **18**, 9955–9964.

45 Y. S. Ryou, J. Lee, H. Lee, C. H. Kim and D. H. Kim, *Catal. Today*, 2017, **320**, 175–180.

46 The Elements Handbook at KnowledgeDoor, http://www.knowledgedoor.com/2/elements_handbook/cohesive_energy.html.

47 S. Krüger, S. Vent and N. Rösch, *Berichte der Bunsengesellschaft für Phys. Chemie*, 1997, **101**, 1640–1643.

48 G. L. Estiu and M. C. Zerner, *J. Phys. Chem.*, 1994, **98**, 4793–4799.

49 M. D. Morse, *Chem. Rev.*, 1986, **86**, 1049–1109.

50 R. Grybos, L. Benco, T. Bučko and J. Hafner, *J. Chem. Phys.*, 2009, **130**, 104503.

51 A. E. Reed and F. Weinhold, *J. Chem. Phys.*, 1983, **78**, 4066–4073.

52 A. E. Reed, B. Weinstock and F. Weinhold, *J. Chem. Phys.*, 1985, **83**, 735–746.

53 A. E. Reed, L. A. Curtiss and F. Weinhold, *Chem. Rev.*, 1988, **88**, 899–926.

54 A. J. W. Thom, E. J. Sundstrom and M. Head-Gordon, *Phys. Chem. Chem. Phys.*, 2009, **11**, 11297.

55 J. A. Panetier, C. S. Letko, T. D. Tilley and M. Head-Gordon, *J. Chem. Theory Comput.*, 2016, **12**, 223–230.

56 J. Pipek and P. Mezey, *J. Chem. Phys.*, 1989, **90**, 4916–4926.

57 J. Pipek and P. Mezey, *Int. J. Quantum Chem.*, 1988, **34**, 1–13.

58 P.-O. Löwdin, *J. Chem. Phys.*, 1950, **18**, 365–375.

59 P.-O. Löwdin, *Phys. Rev.*, 1955, **97**, 1474–1489.

60 H. Li, C. Paolucci, I. Khurana, L. Wilcox, F. Göltl, J. Albarracin-Caballero, A. Shih, F. Ribeiro, R. Gounder, W. Schneider, *Chem. Sci.*, 2018, **10**, 2373–2384.

61 S. C. Larsen, A. Aylor, A. T. Bell and J. A. Reimer, *J. Phys. Chem.*, 1994, **98**, 11533–11540.

62 A. Godiksen, P. N. R. Vennestrøm, S. B. Rasmussen, S. Mossin, *Top. Catal.*, 2017, **60**, 13–29.

63 A. Godiksen, F. N. Stappen, P. N. R. Vennestrøm, F. Giordanino, S. B. Rasmussen, L. F. Lundegaard and S. Mossin, *J. Phys. Chem. C*, 2014, **118**, 23126–23138.

SUPPLEMENTARY INFORMATION

Computational Modeling Predicts the Stability of Both Pd^{+} and Pd^{2+} Ion-Exchanged into H-CHA

Jeroen Van der Mynsbrugge[a], Martin Head-Gordon[b] and Alexis T. Bell[a]*

[a]Department of Chemical and Biomolecular Engineering

University of California, Berkeley, CA 94720, USA

[b]Department of Chemistry

University of California, Berkeley, CA 94720, USA

November 13, 2020

*To whom correspondence should be addressed: alexbell@berkeley.edu

1 Configurational search

Figure S1 illustrates the existence of various chemically equivalent but structurally different configurations for the H^+, Pd^0H^+ and Pd^+ species at isolated Al atoms, and for H^+/H^+, Pd^0 H^+/H^+, Pd^+/H^+ and Pd^{2+} species at the proximate Al pairs. For a given Al, three of its adjacent oxygen atoms are accessible from the CHA cage. The charge compensating H^+ (and therefore the coordinating Pd in Pd^0 H^+) can be located in three different positions. Similarly, Pd^+ can assume two different orientations, facing either the 6-ring or an adjacent 8-ring. While the configuration of Pd^{2+} is trivial, as it is expected to be located near the center of the 6-ring shared by the Al pair responsible for the counter charge, this is not the case for any of the other species. To identify the lowest-free energy structure for each of H^+, Pd^0H^+ and Pd^+ species at isolated Al atoms, and for H^+/H^+, Pd^0 H^+/H^+, Pd^+/H^+ and Pd^{2+} species at the proximate Al pairs in the 6-ring, we have examined all of the configurations that are schematically represented in Figure S1. Their relative free energies are shown in Table S1.

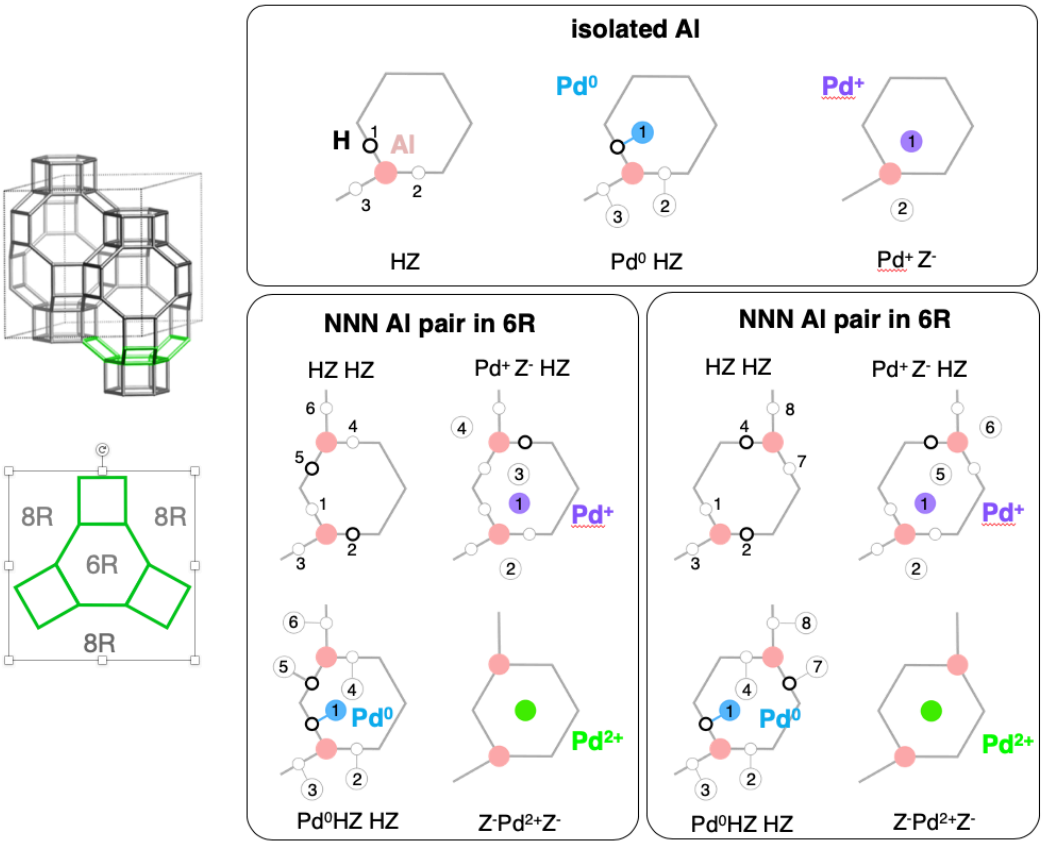

Figure S1. Schematic representation of the various chemically equivalent but structurally different configurations for Pd^{n+} (n=0,1,2) sites at isolated Al and proximate Al pairs in the 6-ring in CHA.

Table S1. Relative free energies (in kJ/mol) of the various chemically equivalent but structurally different configurations for Pd^{n+} (n=0,1,2) sites at isolated Al and proximate Al pairs in the 6-ring in CHA. LOT: ωB97X-D/def2-tzvpd // ωB97X-D/def2-sv(p); T=300 K, P=P_{atm}.

Isolated Al	
HZ	
h1	0
h2	+1
h3	+11
Pd^0 HZ	
h1-pd01	0
h2-pd02	+5
h3-pd03	+9
Pd^+Z^-	
pd11	0
pd12	+7
NNN Al pair	
HZ HZ	
h1-h4	+22
h1-h5	+35
h1-h6	+20
h2-h4	+44
h2-h5	0
h2-h6	+37
h3-h4	+40
h3-h5	+23
h3-h6	+49
Pd^0 HZ HZ	
h1-h4-pd01	+3
h1-h4-pd04	+3
h1-h5-pd01	0
h1-h5-pd05	+24
h1-h6-pd01	+8
h1-h6-pd06	+15
h2-h4-pd02	+37
h2-h4-pd04	+21
h2-h5-pd02	+4
h2-h5-pd05	+3
h2-h6-pd02	+34
h2-h6-pd06	+20

h3-h4-pd03	+34
h3-h4-pd04	+32
h3-h5-pd03	+8
h3-h5-pd05	+26
h3-h6-pd03	+41
h3-h6-pd06	+37
Pd^{+} Z^{-} HZ	
h1-pd13	+43
h1-pd14	+48
h2-pd13	+50
h2-pd14	+48
h3-pd13	+38
h3-pd14	+68
h4-pd11	+75
h4-pd12	+69
h5-pd11	0
h5-pd12	+36
h6-pd11	+39
h6-pd12	+73
NNNN Al pair	
HZ HZ	
h1-h4	+44
h1-h7	0
h1-h8	+20
h2-h4	0
h2-h7	+34
h2-h8	+26
h3-h4	+21
h3-h7	+26
h3-h8	+41
Pd^{0} HZ HZ	
h1-h4-pd01	+16
h1-h4-pd04	+15
h1-h7-pd01	0
h1-h7-pd07	+13
h1-h8-pd01	+20
h1-h8-pd08	+20
h2-h4-pd02	+13
h2-h4-pd04	+2
h2-h7-pd02	+39

h2-h7-pd07	+41
h2-h8-pd02	+38
h2-h8-pd08	+34
h3-h4-pd03	+20
h3-h4-pd04	+20
h3-h7-pd03	+35
h3-h7-pd07	+43
h3-h8-pd03	+45
h3-h8-pd08	+44
Pd^{+} Z^{-} HZ	
h1-pd15	+38
h1-pd16	+14
h2-pd15	0
h2-pd16	+37
h3-pd15	+4
h3-pd16	+42
h4-pd11	+37
h4-pd12	+15
h7-pd11	+1
h7-pd12	+36
h8-pd11	+4
h8-pd12	+42

2 Characteristic Pd-O distances for Pd^{2+}, $Pd^{+}H^{+}$ and $[Pd\text{-}O\text{-}Pd]^{2+}$

Table S2 compares the characteristic Pd-O distances in our model structures for Pd^{2+}, $Pd^{+}H^{+}$ and $[Pd\text{-}O\text{-}Pd]^{2+}$ at the NNNN Al pair in the 6-ring with those reported by Khivantsev et al. (ref. 17 in the main text) and Paolucci et al. (ref. 23 in the main text), showing excellent agreement despite the use of different computational methods.

Table S2. Comparison of the characteristic Pd-O distances in our model structures for Pd^{2+}, $Pd^{+}H^{+}$ and $[Pd\text{-}O\text{-}Pd]^{2+}$ at the NNNN Al pair in the 6-ring with those in similar structures reported by Khivantsev et al. (ref. 17 in the main text) and Paolucci et al. (ref. 23 in the main text).

	d(Pd-O_{zeo}) [Å]		
	This study	*Khivantsev et al.*[17]	*Paolucci et al.*[32]
Pd^{2+}	2.04; 2.04; 2.11; 2.11	2.06; 2.06; 2.14; 2.14	2.04; 2.04; 2.11; 2.11
Pd^{+}	2.23; 2.30; 2.33; 2.33	2.20; 2.22; 2.25	2.18–2.38
$[Pd\text{-}O\text{-}Pd]^{2+}$	2.10; 2.17; 2.11; 2.18	2.14; 2.19; 2.14; 2.19	

3 Validation of the QM region selections

To validate our choice of QM regions used to model Pd sites at the different proximate Al pairs in the 6-ring or 8-ring, additional test calculations were performed using the larger QM regions shown in Figure S2, which include the full 6-ring and 8-ring for all Al pairs. To ensure that the salient observations discussed in the main text are unaffected if only the ring in which both Al atoms are located is treated at the QM level, we have reoptimized the structures of $Pd^{+}H^{+}Z^{-}Z^{-}$ and $Pd^{2+}Z^{-}Z^{-}$ using the alternative QM regions and evaluated the effect of the QM region on the energies of formation of $Pd^{+}H^{+}Z^{-}Z^{-}$ and $Pd^{2+}Z^{-}Z^{-}$,which were ultimately found to be the most favorable species over a wide range of operating conditions for all Al pairs. The results of these calculations are shown in Figure S3 and Table S2.The same trends are obtained regardless of the QM region,

and crucially the *difference* in formation energy between $Pd^{+}H^{+}Z^{-}Z^{-}$ and $Pd^{2+}Z^{-}Z^{-}$ is reproduced within 12 kJ/mol or less (Table S2).

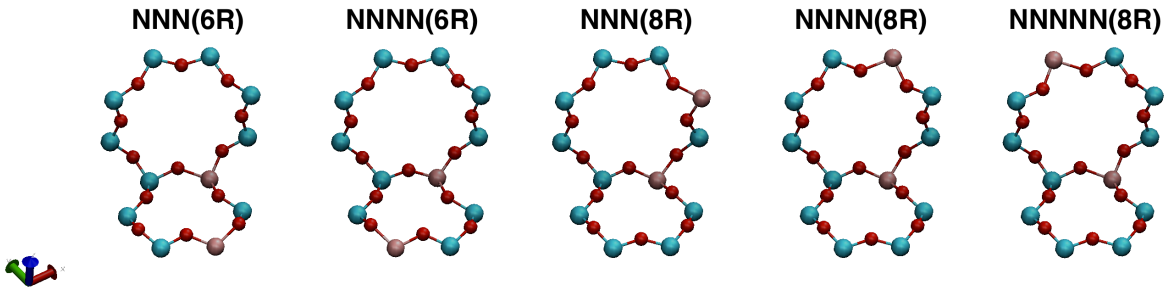

Figure S2. Alternative QM regions including both the 6-ring and the 8-ring for different proximate Al pairs in the 6-ring (NNN and NNNN) or 8-ring (NNN, NNNN and NNNNN). Si atoms are shown in cyan, Al in pink, O in red, H in white

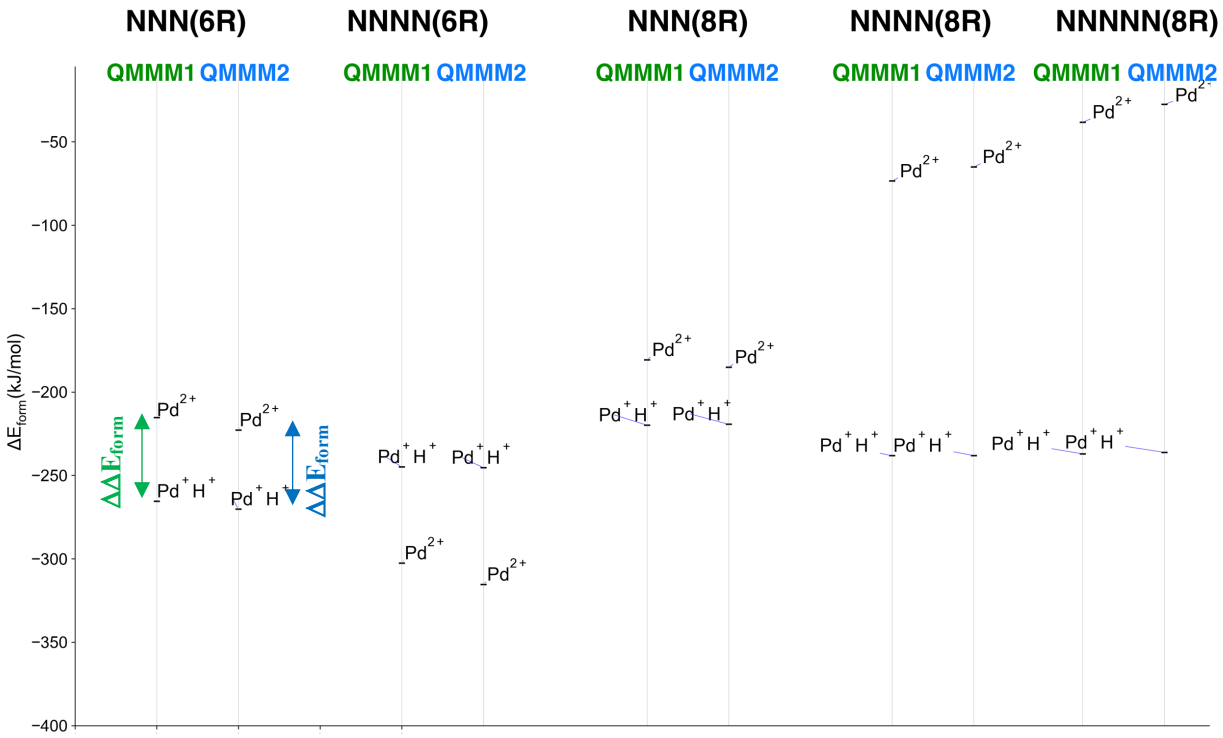

Figure S3. Formation energies of $Pd^{+}H^{+}Z^{-}Z^{-}$ and $Pd^{2+}Z^{-}Z^{-}$ at the different Al pairs in the 6-ring or 8-ring, evaluated at the ωB97X-D/def2-tzvpd // ωB97X-D/def2-sv(p) level of theory using the QM regions shown in Figure 1 in the main text (QMMM1) and using the alternative QM regions shown in Figure S2 (QMMM2).

Table S2. Differences in formation energies of $Pd^{+}H^{+}Z^{-}Z^{-}$ and $Pd^{2+}Z^{-}Z^{-}$ at the different Al pairs in the 6-ring or 8-ring, evaluated at the ωB97X-D/def2-tzvpd // ωB97X-D/def2-sv(p) level of theory using the QM regions shown in Figure 1 in the main text (QMMM1) and using the alternative QM regions shown in Figure S2 (QMMM2).

	$\Delta\Delta E_{form}(Pd^{+}H^{+}Z^{-}Z^{-} - Pd^{2+}Z^{-}Z^{-})$		
	QMMM1 kJ/mol	**QMMM2** kJ/mol	**|QMMM1 – QMMM2|** kJ/mol
NNN(6R)	-50	-47	3
NNNN(6R)	58	70	12
NNN(8R)	-39	-34	5
NNNN(8R)	-165	-173	8
NNNNN(8R)	-199	-209	10

4 Validation of the density functional selection

Additionally, we have evaluated the energies of formation of $Pd^{+}H^{+}Z^{-}Z^{-}$ and $Pd^{2+}Z^{-}Z^{-}$ using the wB97M-V functional to refine the energies of the structures of $Pd^{+}H^{+}Z^{-}Z^{-}$ and $Pd^{2+}Z^{-}Z^{-}$ obtained with the QM regions shown in Figure 1 in the main text to assess the effect of our choice of density functional. The results of these calculations are shown in Figure S4 and Table S3. Again, the same trends are obtained with either functional, and the difference in formation energy between $Pd^{+}H^{+}Z^{-}Z^{-}$ and $Pd^{2+}Z^{-}Z^{-}$ is reproduced within 9 kJ/mol or less (Table S3).

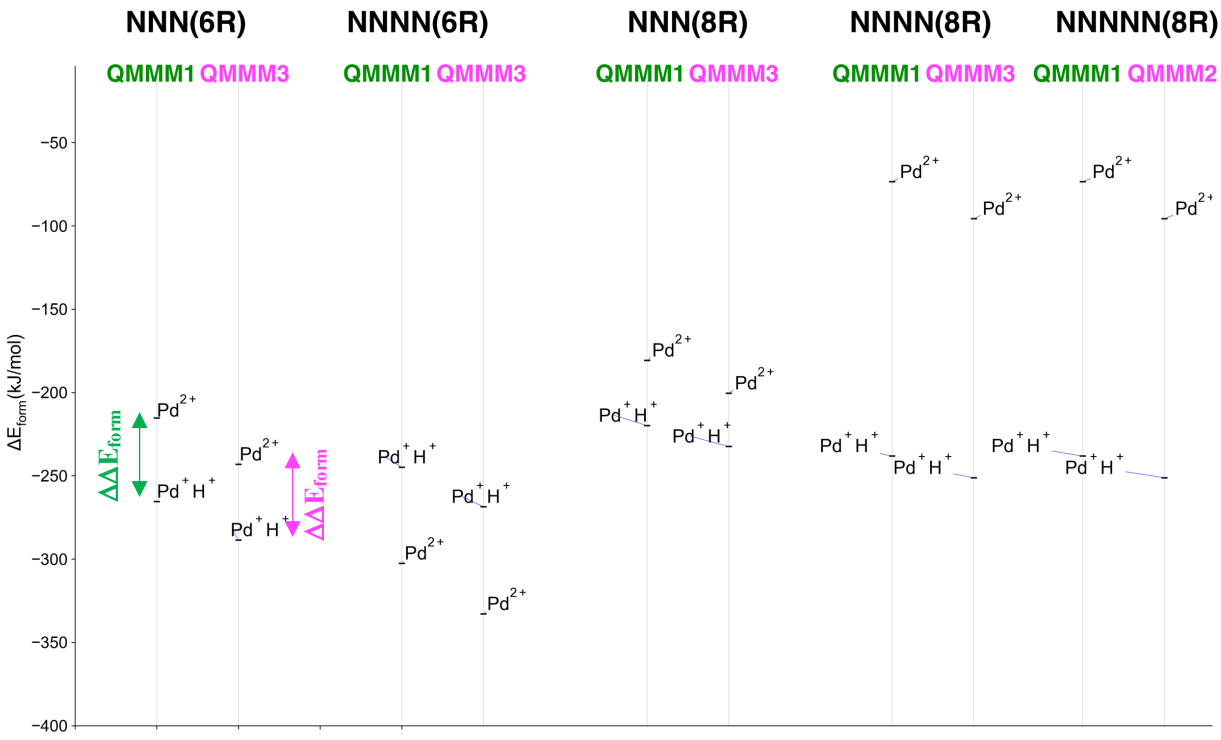

Figure S4. Formation energies of $Pd^{+}H^{+}Z^{-}Z^{-}$ and $Pd^{2+}Z^{-}Z^{-}$ at the different Al pairs in the 6-ring or 8-ring, evaluated using the QM regions shown in Figure 1 in the main text at the ωB97X-D/def2-tzvpd // ωB97X-D/def2-sv(p) level of theory (QMMM1) and at the ωB97M-V/def2-tzvpd // ωB97X-D/def2-sv(p) level of theory (QMMM3).

Table S3. Differences in formation energies of $Pd^{+}H^{+}Z^{-}Z^{-}$ and $Pd^{2+}Z^{-}Z^{-}$ at the different Al pairs in the 6-ring or 8-ring, evaluated using the QM regions shown in Figure 1 in the main text at the ωB97X-D/def2-tzvpd // ωB97X-D/def2-sv(p) level of theory (QMMM1) and at the ωB97M-V/def2-tzvpd // ωB97X-D/def2-sv(p) level of theory (QMMM3).

	$\Delta\Delta E_{form}(Pd^{+}H^{+}Z^{-}Z^{-} - Pd^{2+}Z^{-}Z^{-})$		
	QMMM1 kJ/mol	QMMM3 kJ/mol	|QMMM1 – QMMM3| kJ/mol
NNN(6R)	-50	-46	4
NNNN(6R)	58	64	7
NNN(8R)	-39	-32	7
NNNN(8R)	-165	-156	9
NNNNN(8R)	-199	-193	6

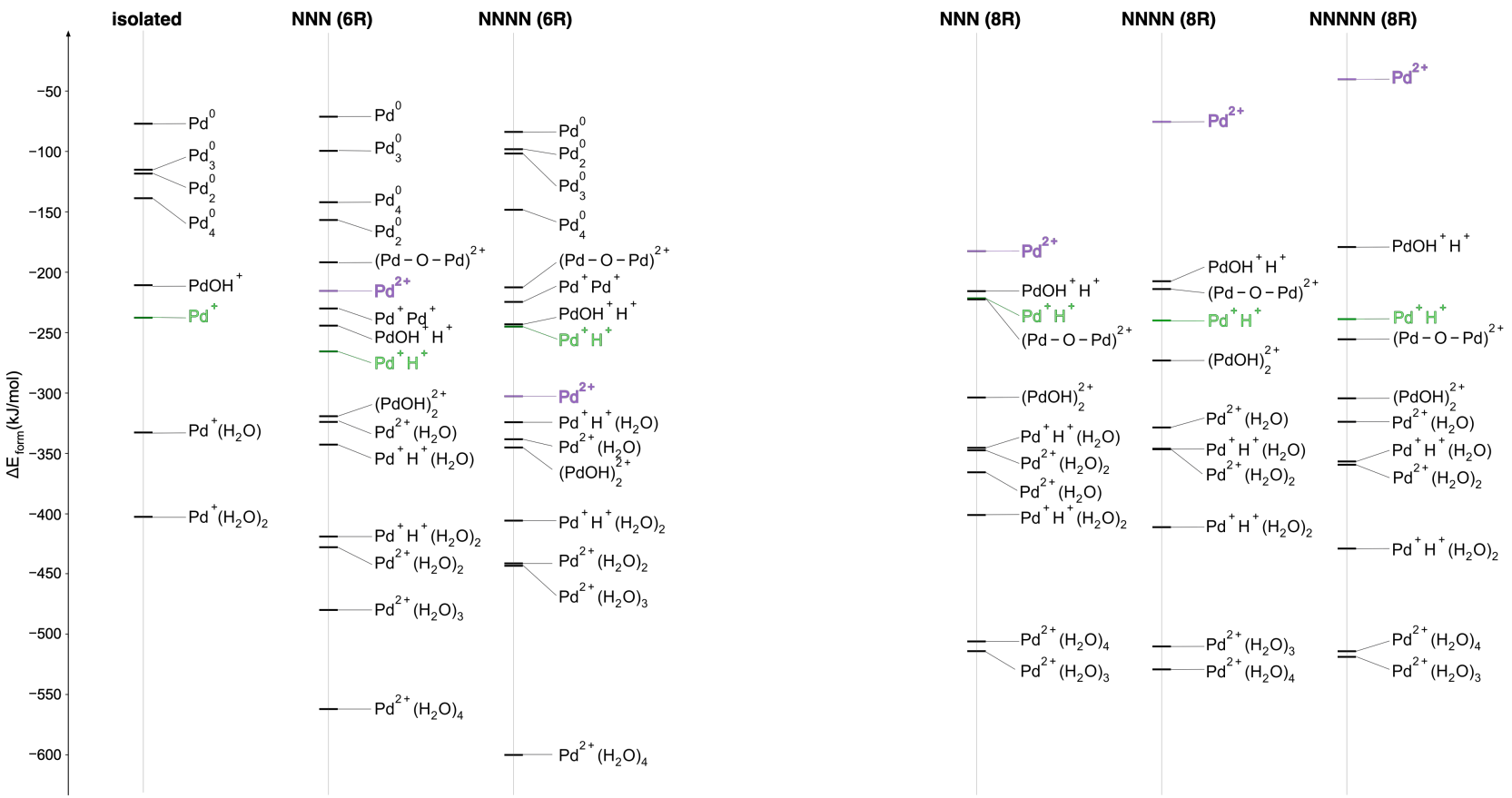

Figure S5. Electronic energies of formation (ΔE_{form}) for the Pd species in both the 6-ring (ΔG_{form} in Figure 4 of main text) and in the 8-ring (ΔG_{form} in Figure 8 of main text).

5 Phase diagrams

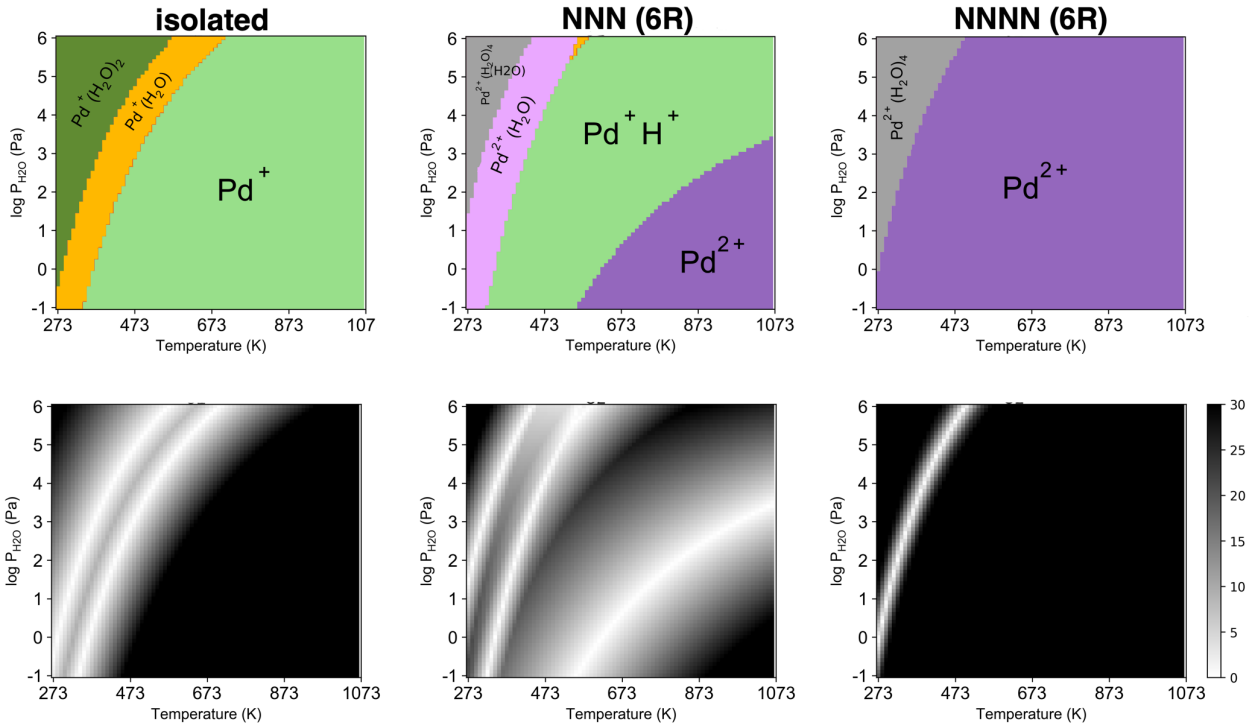

Figure S6. [P_{H2O},T] phase diagrams showing the thermodynamically preferred Pd species (top row; Figure 5 in the main text) and corresponding heat maps (bottom row) illustrating the difference in free energy of formation (in kJ/mol) between the thermodynamically preferred Pd species and the species with the next-lowest free energy at isolated Al and Al pairs – next-next-nearest neighbors (NNNN) and next-nearest neighbors (NNN) – in the 6-ring of H-CHA under flowing air (p_{O2} = 20 kPa).

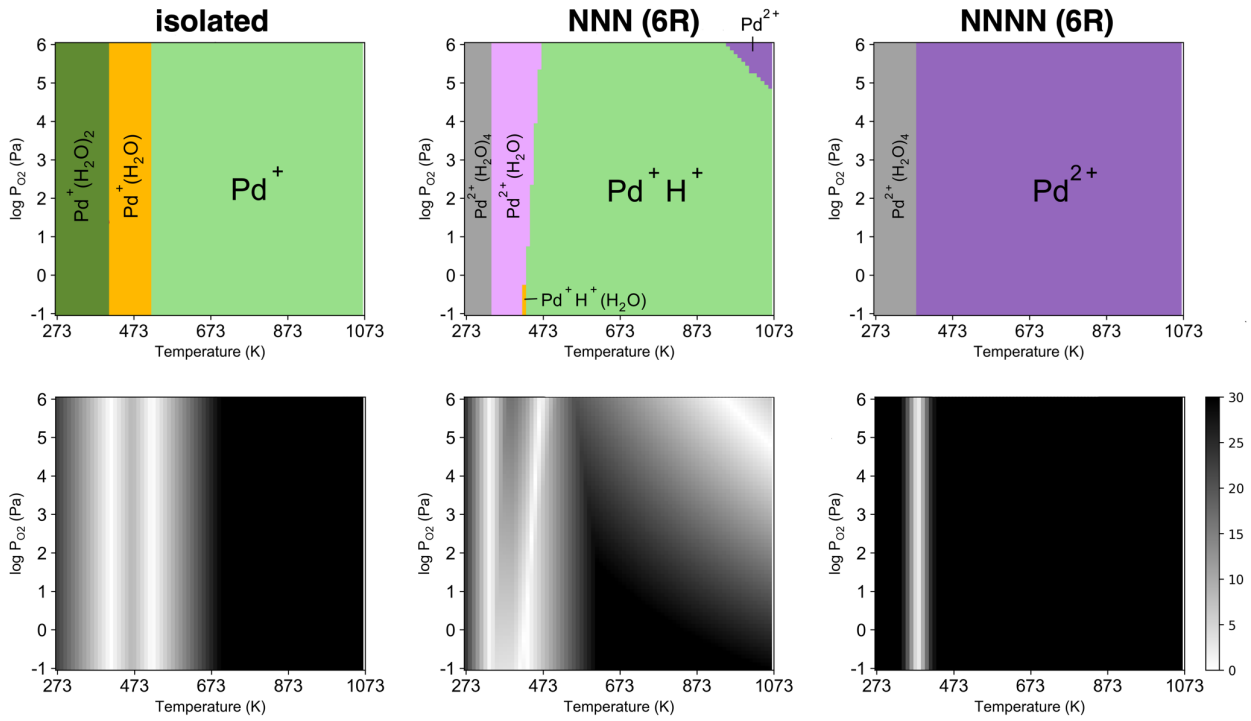

Figure S7. [P_{O2},T] phase diagrams showing the thermodynamically preferred Pd species (top row) and corresponding heat maps (bottom row) illustrating the difference in free energy of formation (in kJ/mol) between the thermodynamically preferred Pd species and the species with the next-lowest free energy at isolated Al and Al pairs – next-next-nearest neighbors (NNNN) and next-nearest neighbors (NNN) – in the 6-ring of H-CHA under oxidizing conditions with 5% water (p_{H2O} = 5 kPa).

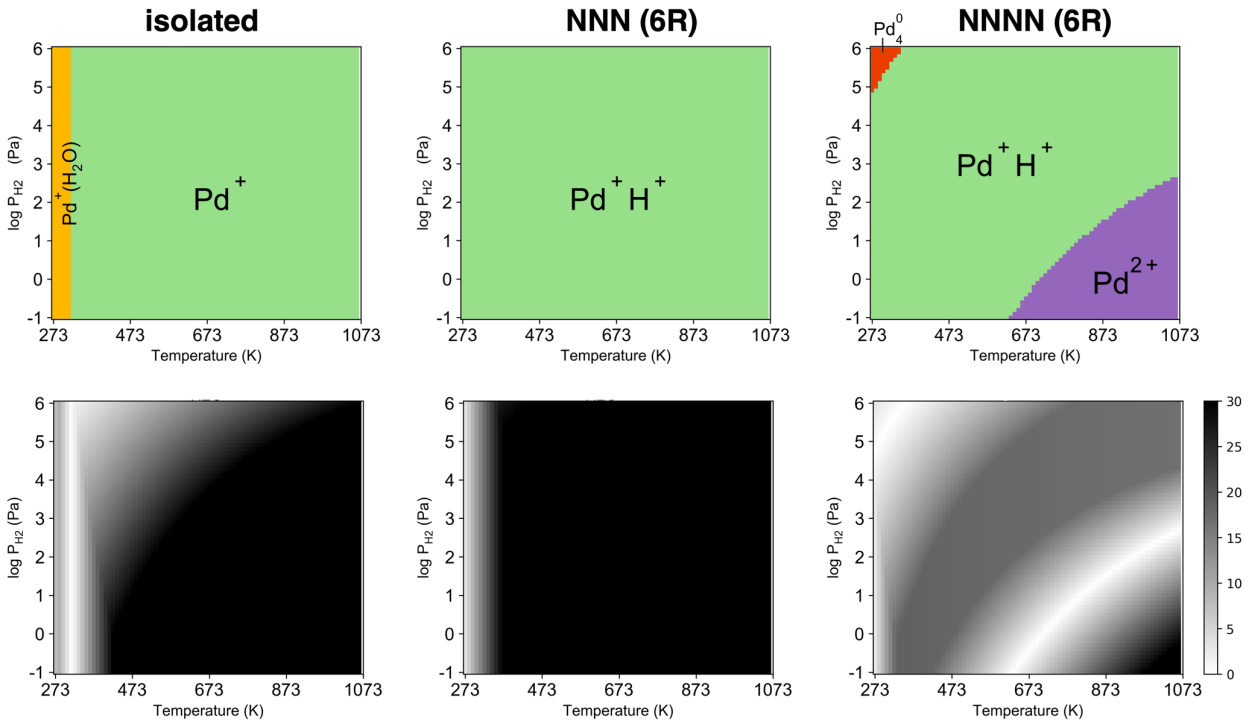

Figure S8. [P_{H2},T] phase diagrams showing the thermodynamically preferred Pd species (top row; Figure 7 in the main text) and corresponding heat maps (bottom row) illustrating the difference in free energy of formation (in kJ/mol) between the thermodynamically preferred Pd species and the species with the next-lowest free energy at isolated Al and Al pairs – next-next-nearest neighbors (NNNN) and next-nearest neighbors (NNN) – in the 6-ring of H-CHA under dry reducing conditions (p_{H2O} = 0.01 Pa).

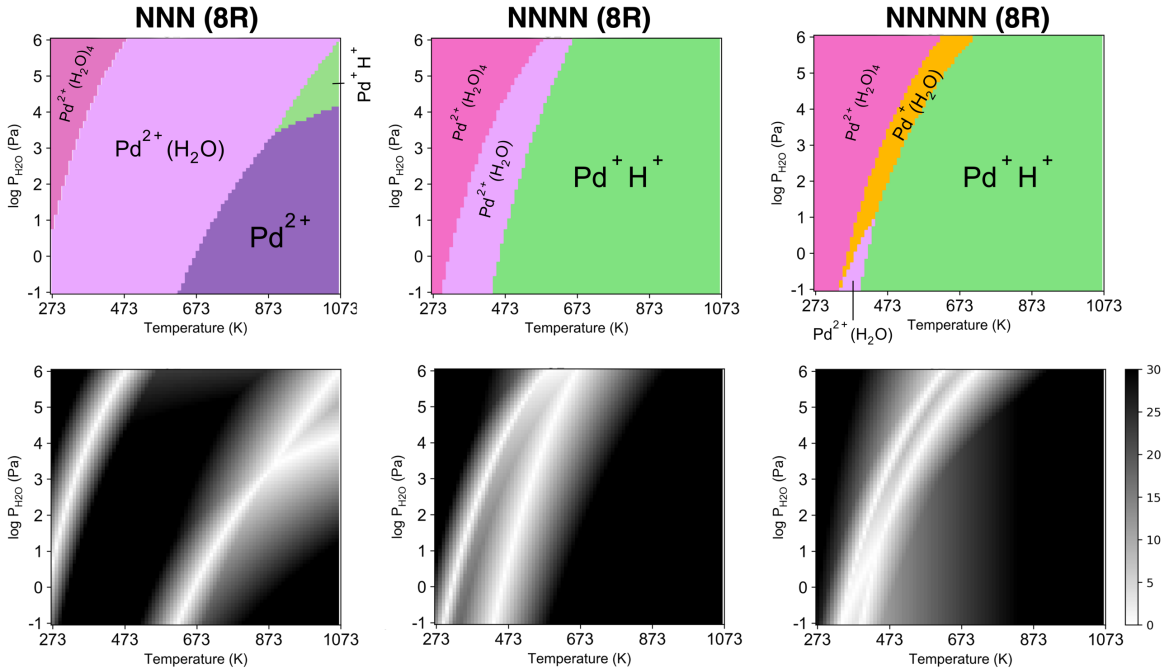

Figure S9. [P_{H2O},T] phase diagrams showing the thermodynamically preferred Pd species (top row; Figure 9 in the main text) and corresponding heat maps (bottom row) illustrating the difference in free energy of formation (in kJ/mol) between the thermodynamically preferred Pd species and the species with the next-lowest free energy at next-nearest neighbors (NNN), next-next-nearest neighbors (NNNN), next-next-next-nearest neighbors (NNNNN) Al pairs in the 8-ring of H-CHA under flowing air (p_{O2} = 20 kPa).

6 Alternative 3D representations of select structures

Because of the nature of the CHA (a dense 3D network of interconnected cages) it is difficult to show the active sites in their framework context in a single 2D representation without confusing the reader. For this reason, we have opted to omit the MM atoms in the Figures included in the manuscript. Below are a few additional figures showing an alternative representation for a selection of structures. The QM atoms are shown in ball-and-stick representation; the remaining atoms of the central *cha* cage are shown as a bolder wireframe for visual clarity (as in Figure 1 in the main text).

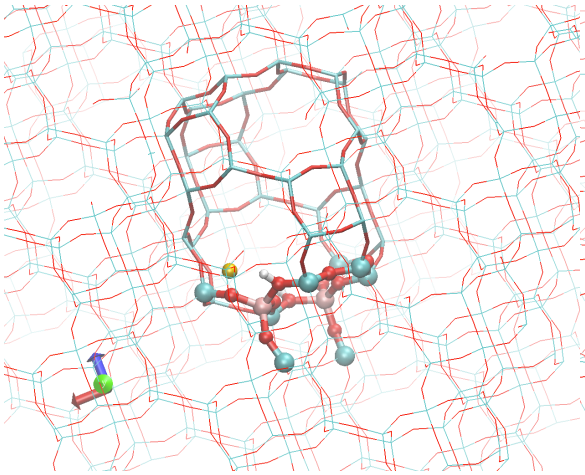

HZ Pd^0 HZ NNN(6R)

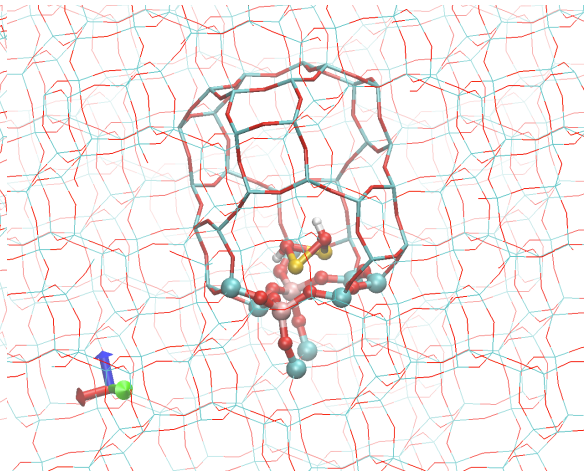

Z^- $(PdOH)_2^{2+}$ Z^- NNN(6R)

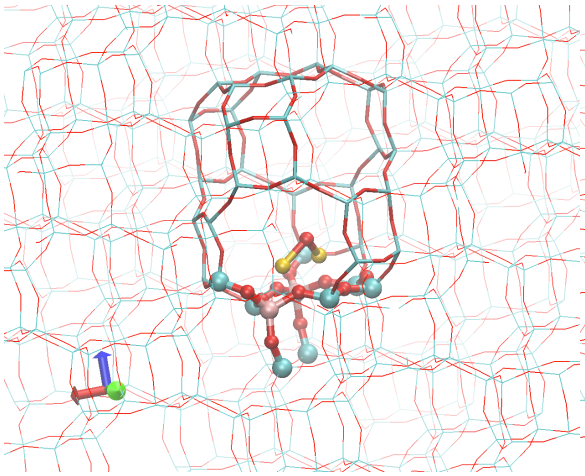

Z^- $(Pd\text{-}O\text{-}Pd)^{2+}$ Z^- NNN(6R)

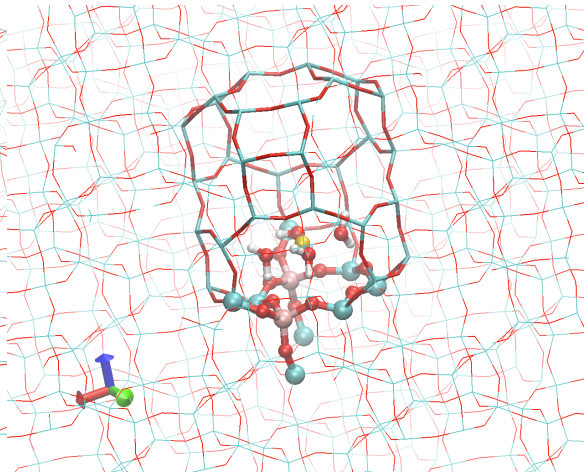

Z^- $Pd^{2+}(H_2O)_4$ Z^- NNN(6R)

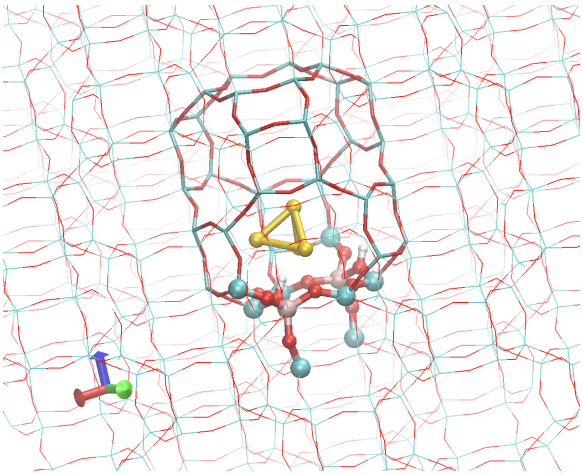

HZ Pd_4^0 HZ NNNN(6R)

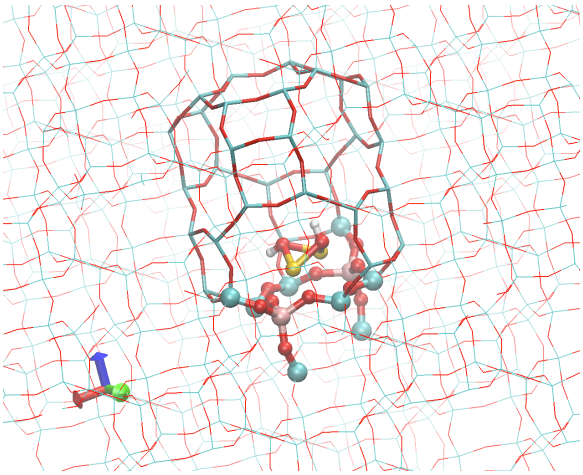

Z^- $(PdOH)_2^{2+}$ Z^- NNNN(6R)

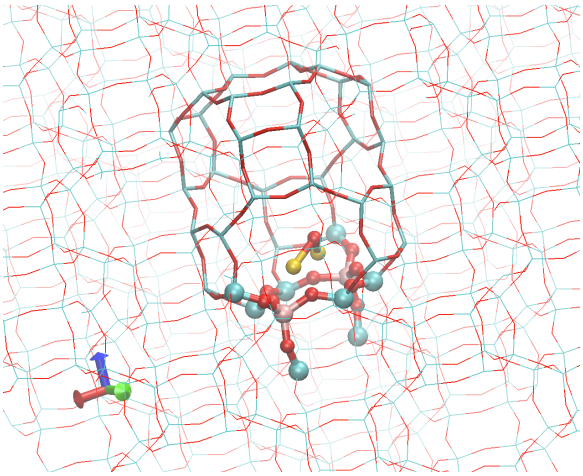

Z^- $(Pd\text{-}O\text{-}Pd)^{2+}$ Z^- NNN(6R)

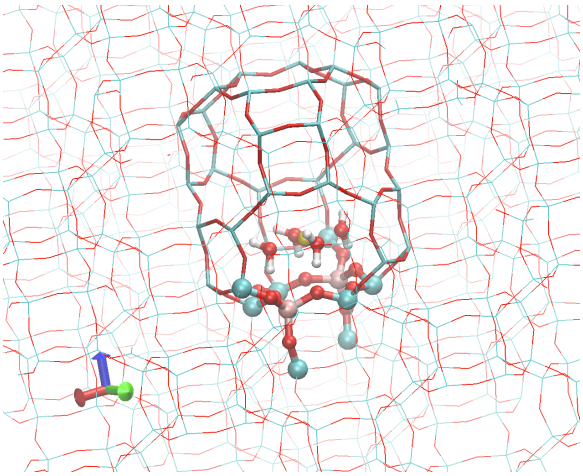

Z^- $Pd^{2+}(H_2O)_4$ Z^- NNN(6R)

7 XYZ coordinates of all stationary points

See ZIP archive; QM atoms are grouped at the top of each geometry.

Description	Filename	# QM atoms
isolated Al		
HZ	001.xyz	17
Pd^0 HZ	002.xyz	18
Pd_2^0 HZ	003.xyz	19
Pd_3^0 HZ	004.xyz	20
Pd_4^0 HZ	005.xyz	21
Pd^+ Z^-	006.xyz	17
$Pd^+(H_2O)$ Z^-	007.xyz	20
$Pd^+(H_2O)_2$ Z^-	008.xyz	23
$PdOH^+$ Z^-	009.xyz	19
NNN(6R)		
HZ HZ	010.xyz	22
HZ Pd^0 HZ	011.xyz	23
HZPd_2^0 HZ (Z$^-$ Pd_2H^+ HZ)	012.xyz	24
HZ Pd_3^0 HZ	013.xyz	25
HZ Pd_4^0 HZ	014.xyz	26
HZ Pd^+ Z^-	015.xyz	22
HZ $Pd^+(H_2O)$ Z^-	016.xyz	25
HZ $Pd^+(H_2O)_2$ Z^-	017.xyz	28
Z^-Pd^+ Pd^+Z^-	018.xyz	22
Z^- Pd^{2+} Z^-	019.xyz	21
Z^- $Pd^{2+}(H_2O)$ Z^-	020.xyz	24
Z^- $Pd^{2+}(H_2O)_2$ Z^-	021.xyz	27
Z^- $Pd^{2+}(H_2O)_3$ Z^-	022.xyz	30
Z^- $Pd^{2+}(H_2O)_4$ Z^-	023.xyz	33
HZ $PdOH^+$ Z^-	024.xyz	24
Z^- $(PdOH)_2^{2+}$ Z^-	025.xyz	26
Z^- $(Pd\text{-}O\text{-}Pd)^{2+}$ Z^-	026.xyz	23
NNNN(6R)		
HZ HZ	027.xyz	22
HZ Pd^0 HZ	028.xyz	23
HZPd_2^0 HZ	029.xyz	24
HZ Pd_3^0 HZ	030.xyz	25
HZ Pd_4^0 HZ	031.xyz	26
HZ Pd^+ Z^-	032.xyz	22
HZ $Pd^+(H_2O)$ Z^-	033.xyz	25
HZ $Pd^+(H_2O)_2$ Z^-	034.xyz	28

$Z^{-}Pd^{+}$ $Pd^{+}Z^{-}$	035.xyz	22
Z^{-} Pd^{2+} Z^{-}	036.xyz	21
Z^{-} $Pd^{2+}(H_2O)$ Z^{-}	037.xyz	24
Z^{-} $Pd^{2+}(H_2O)_2$ Z^{-}	038.xyz	27
Z^{-} $Pd^{2+}(H_2O)_3$ Z^{-}	039.xyz	30
Z^{-} $Pd^{2+}(H_2O)_4$ Z^{-}	040.xyz	33
HZ $PdOH^{+}$ Z^{-}	041.xyz	24
Z^{-} $(PdOH)_2^{2+}$ Z^{-}	042.xyz	26
Z^{-} $(Pd\text{-}O\text{-}Pd)^{2+}$ Z^{-}	043.xyz	23
NNN(8R)		
HZ HZ	044.xyz	26
HZ Pd^{+} Z^{-}	045.xyz	26
HZ $Pd^{+}(H_2O)$ Z^{-}	046.xyz	29
HZ $Pd^{+}(H_2O)_2$ Z^{-}	047.xyz	32
Z^{-} Pd^{2+} Z^{-}	048.xyz	25
Z^{-} $Pd^{2+}(H_2O)$ Z^{-}	049.xyz	28
Z^{-} $Pd^{2+}(H_2O)_2$ Z^{-}	050.xyz	31
Z^{-} $Pd^{2+}(H_2O)_3$ Z^{-}	051.xyz	34
Z^{-} $Pd^{2+}(H_2O)_4$ Z^{-}	052.xyz	37
HZ $PdOH^{+}$ Z^{-}	053.xyz	28
Z^{-} $(PdOH)_2^{2+}$ Z^{-}	054.xyz	30
Z^{-} $(Pd\text{-}O\text{-}Pd)^{2+}$ Z^{-}	055.xyz	27
NNNN(8R)		
HZ HZ	056.xyz	26
HZ Pd^{+} Z^{-}	057.xyz	26
HZ $Pd^{+}(H_2O)$ Z^{-}	058.xyz	29
HZ $Pd^{+}(H_2O)_2$ Z^{-}	059.xyz	32
Z^{-} Pd^{2+} Z^{-}	060.xyz	25
Z^{-} $Pd^{2+}(H_2O)$ Z^{-}	061.xyz	28
Z^{-} $Pd^{2+}(H_2O)_2$ Z^{-}	062.xyz	31
Z^{-} $Pd^{2+}(H_2O)_3$ Z^{-}	063.xyz	34
Z^{-} $Pd^{2+}(H_2O)_4$ Z^{-}	064.xyz	37
HZ $PdOH^{+}$ Z^{-}	065.xyz	28
Z^{-} $(PdOH)_2^{2+}$ Z^{-}	066.xyz	30
Z^{-} $(Pd\text{-}O\text{-}Pd)^{2+}$ Z^{-}	067.xyz	27
NNNNN(8R)		
HZ HZ	068.xyz	26
HZ Pd^{+} Z^{-}	069.xyz	26
HZ $Pd^{+}(H_2O)$ Z^{-}	070.xyz	29
HZ $Pd^{+}(H_2O)_2$ Z^{-}	071.xyz	32
Z^{-} Pd^{2+} Z^{-}	072.xyz	25
Z^{-} $Pd^{2+}(H_2O)$ Z^{-}	073.xyz	28

$Z^- Pd^{2+}(H_2O)_2 Z^-$	074.xyz	31
$Z^- Pd^{2+}(H_2O)_3 Z^-$	075.xyz	34
$Z^- Pd^{2+}(H_2O)_4 Z^-$	076.xyz	37
$HZ\ PdOH^+ Z^-$	077.xyz	28
$Z^- (PdOH)_2^{2+} Z^-$	078.xyz	30
$Z^- (Pd\text{-}O\text{-}Pd)^{2+} Z^-$	079.xyz	27

Other files

XYZ files.zip (1.44 MiB) view on ChemRxiv • download file